Carbon Monitoring Satellite (CarbonSat): assessment of atmospheric CO_2 and CH_4 retrieval errors by error parameterization

M. Buchwitz[1], M. Reuter[1], H. Bovensmann[1], D. Pillai[1], J. Heymann[1], O. Schneising[1], V. Rozanov[1], T. Krings[1], J. P. Burrows[1], H. Boesch[2], C. Gerbig[3], Y. Meijer[4], and A. Löscher[4]

[1]Institute of Environmental Physics (IUP), University of Bremen FB1, Otto Hahn Allee 1, 28334 Bremen, Germany
[2]Department of Physics and Astronomy, University of Leicester, Leicester, UK
[3]Max-Planck-Institute for Biogeochemistry (MPI-BGC), Jena, Germany
[4]ESA ESTEC, Noordwijk, the Netherlands

Correspondence to: M. Buchwitz (michael.buchwitz@iup.physik.uni-bremen.de)

Abstract. Carbon Monitoring Satellite (CarbonSat) is one of two candidate missions for ESA's Earth Explorer 8 (EE8) satellite to be launched around the end of this decade. The overarching objective of the CarbonSat mission is to improve our understanding of natural and anthropogenic sources and sinks of the two most important anthropogenic greenhouse gases (GHGs) carbon dioxide (CO_2) and methane (CH_4). The unique feature of CarbonSat is its "GHG imaging capability", which is achieved via a combination of high spatial resolution ($2\,km \times 2\,km$) and good spatial coverage (wide swath and gap-free across- and along-track ground sampling). This capability enables global imaging of localized strong emission source, such as cities, power plants, methane seeps, landfills and volcanos, and likely enables better disentangling of natural and anthropogenic GHG sources and sinks. Source–sink information can be derived from the retrieved atmospheric column-averaged mole fractions of CO_2 and CH_4, i.e. XCO_2 and XCH_4, by inverse modelling. Using the most recent instrument and mission specification, an error analysis has been performed using the Bremen optimal EStimation DOAS (BESD/C) retrieval algorithm. We assess the retrieval performance for atmospheres containing aerosols and thin cirrus clouds, assuming that the retrieval forward model is able to describe adequately all relevant scattering properties of the atmosphere. To compute the errors for each single CarbonSat observation in a one-year period, we have developed an error parameterization scheme comprising six relevant input parameters: solar zenith angle, surface albedo in two bands, aerosol and cirrus optical depth, and cirrus altitude variations. Other errors, e.g. errors resulting from aerosol type variations, are partially quantified but not yet accounted for in the error parameterization. Using this approach, we have generated and analysed one year of simulated CarbonSat observations. Using this data set we estimate that systematic errors are for the overwhelming majority of cases ($\approx 85\,\%$) below 0.3 ppm for XCO_2 (below 0.5 ppm for 99.5 %) and below 2 ppb for XCH_4 (below 4 ppb for 99.3 %). We also show that the single-measurement precision is typically around 1.2 ppm for XCO_2 and 7 ppb for XCH_4 (1σ). The number of quality-filtered observations over cloud- and ice-free land surfaces is in the range of 33 to 47 million per month depending on season. Recently it has been shown that terrestrial vegetation chlorophyll fluorescence (VCF) emission needs to be considered for accurate XCO_2 retrieval. We therefore retrieve VCF from clear Fraunhofer lines located around 755 nm and show that CarbonSat will provide valuable information on VCF. We estimate that the VCF single-measurement precision is approximately $0.3\,mW\,m^{-2}\,nm^{-1}\,sr^{-1}$ (1σ).

1 Introduction

Carbon dioxide (CO_2) and methane (CH_4) are the two most important anthropogenic greenhouse gases (GHGs) contributing to global warming (Solomon et al., 2007). Their concentration in the atmosphere has significantly increased during the previous decades and still continues to increase (e.g. Francey et al., 2013; Olivier et al., 2012; Schneising et al., 2011, 2013a, b; Dlugokencky et al., 2009; Rigby et al., 2008; and references given therein). Despite their importance, our knowledge on their sources and sinks has significant gaps (e.g. Kirschke et al., 2013; Bergamaschi et al., 2013; Ciais et al., 2013; Houweling et al., 2013; Canadell et al., 2010; Stephens et al., 2007). For example, Canadell et al. (2010) summarizes the situation as follows for the carbon cycle: "Quantification of carbon sources and sinks, their spatial distribution and evolution over time remain a critical area of research. … At present, uncertainty of national or continental budgets is on the order of 50 % at the best, and around 30 % for global natural fluxes". For methane, the situation is similar (see e.g. Kirschke et al., 2013, and Houweling et al., 2013; and references given therein, for a discussion on recent efforts to identify the reason for the renewed atmospheric methane growth).

Global satellite observations of CO_2 and CH_4 can help to close important knowledge gaps on CO_2 and CH_4 regional-scale sources and sinks (e.g. Guerlet et al., 2013a; Basu et al., 2013; Maksyutov et al., 2012; Bergamaschi et al., 2013; Bergamaschi et al., 2009; Houweling et al., 2013; Rayner and O'Brien, 2001). Knowledge gaps also exist and – depending on the source – may be even larger on smaller scales, e.g. the various local industrial and geological sources of methane (see Krings et al., 2013; Leifer et al., 2013; Bovensmann et al., 2010; and references given therein), for CO_2-emitting power plants (e.g. Krings et al., 2011; Velazco et al., 2011; Bovensmann et al., 2010; and references given therein), and CO_2 emissions from cities or large urban agglomerations (e.g. Schneising et al., 2008, 2013a; Keppel-Aleks et al., 2012; Kort et al., 2012; McKain et al., 2012; Wunch et al., 2009; and references given therein). Satellite observations of GHGs are also required to contribute to the verification of international agreements on emission reductions (e.g. NRC, 2010; and references given therein).

To contribute to the above-mentioned research and application areas, CO_2 and CH_4 data with high precision and accuracy, good spatio-temporal coverage and sensitivity to near-surface concentration variations (e.g. Buchwitz et al., 2011, 2013a; Chevallier et al., 2007; Meirink et al., 2006) are required. The Carbon Monitoring Satellite (CarbonSat) (Bovensmann et al., 2010) mission and instrument concept is addressing these needs. The objective of the CarbonSat mission is to determine and separate natural and anthropogenic CO_2 and CH_4 sources and sinks. CarbonSat will contribute to the quantification of natural fluxes of CO_2 and CH_4 (e.g. biospheric CO_2, wetland CH_4) but also to a much

better estimation of anthropogenic emissions than is possible with any of the other existing or planned satellite missions. This will be achieved via a unique feature of CarbonSat, which is its "GHG imaging capability". GHG imaging is achieved via a combination of high spatial resolution ($2\,km \times 2\,km$) and good spatial coverage. This is achieved by having a relatively wide swath and no gaps between adjacent (across-track and along-track) ground pixels. The width of the across-track swath has not yet been finally decided. Here we present results for two swath widths: $240\,km$ (CarbonSat's breakthrough requirement) and $500\,km$ (goal requirement). This capability enables global imaging of localized strong emission sources, such as cities, power plants, methane seeps, landfills and volcanos, and likely enables a better disentangling of anthropogenic and GHG natural sources and sinks.

The main data products of CarbonSat are atmospheric column-averaged dry air mole fractions of CO_2 and CH_4, denoted by $X CO_2$ and $X CH_4$. These data products are also generated, or are planned to be generated, from other past, present and future GHG missions such as SCIAMACHY (SCanning Imaging Absorption spectroMeter for Atmospheric CHartographY) (Burrows et al., 1995; Bovensmann et al., 1999; Buchwitz et al., 2005), GOSAT (Greenhouse Gases Observing Satellite) (Kuze et al., 2009; Yoshida et al., 2011) and the upcoming OCO-2 (Orbiting Carbon Observatory) mission ($X CO_2$ only) (Crisp et al., 2004; Boesch et al., 2011). Compared to these missions, CarbonSat aims at better disentangling of natural and anthropogenic sources and sinks of CO_2 and CH_4 by using its GHG imaging capability. CarbonSat has been selected by the European Space Agency (ESA) to be one of two candidate missions for ESA's Earth Explorer 8 (EE8) satellite. The other candidate mission is the FLuorscence EXplorer (FLEX) (ESA, 2008). After selection it is planned that one of these competing missions will be launched around the end of this decade (i.e. around 2020).

Near-surface sensitivity is achieved by measuring spectra of solar radiation reflected at the Earth's surface and backscattered into the atmosphere and thus into space using spectral regions sensitive to CO_2 and CH_4 absorption. These spectra are also influenced by atmospheric scattering by air molecules (Rayleigh scattering), aerosols and clouds. Scattering alters the light path and needs to be appropriately accounted for when retrieving CO_2 and CH_4 information from the measured spectra. One focus of this manuscript is to address this aspect. It is well known that unaccounted variability of atmospheric scattering by aerosols and clouds, especially undetected thin cirrus clouds, is a significant error source for the determination of CO_2 and CH_4, retrieved from measurements of the backscattered solar spectra at the top of the atmosphere (e.g. Guerlet et al., 2013b; Heymann et al., 2012a, b; Oshchepkov et al., 2012; O'Dell et al., 2012; Reuter et al., 2011, 2013; Butz et al., 2009, 2011). It is therefore important to assess to what extent a particular type of measurement (here the proposed measurements

of CarbonSat) may suffer from this error source. To evaluate this, we have conducted an assessment by using accurate simulations of CarbonSat observations. We focus on errors resulting from aerosols and cirrus clouds assuming that scenes contaminated by thick clouds have already been identified (e.g. by pre-processing O_2 A-band spectra) and removed (i.e. in a manner similar to that currently used for SCIAMACHY (e.g. Heymann et al., 2012a, b; Reuter et al., 2011) and GOSAT (e.g. Cogan et al., 2012; O'Dell et al., 2012; Crisp et al., 2012; Butz et al., 2011).

Initial error analysis results for CarbonSat concerning aerosols and cirrus clouds have already been presented in Bovensmann et al. (2010). That study focussed on the application of inferring CO_2 emissions of coal-fired power plants from single CarbonSat overpass data. Here we extend this analysis by computing and analysing errors for one year of global simulated CarbonSat observations. For this purpose we have developed an error parameterization method which permits fast computation of random and systematic XCO_2 and XCH_4 errors as a function of several critical input parameters such as aerosol optical depth (AOD), cirrus OD and cirrus altitude. The error analysis is based on the most recent instrument and mission specification and uses the latest version of the BESD/C "full physics" algorithm (Bovensmann et al., 2010) for retrieving geophysical parameters from CarbonSat radiances.

This manuscript is structured as follows: in Sect. 2 the main CarbonSat instrument characteristics are described, and in Sect. 3 the retrieval algorithm is briefly presented, focusing on recent improvements. In Sect. 4 the error analysis and error parameterization approach is described. The error parameterization method permits fast computation of random and systematic XCO_2 and XCH_4 errors and averaging kernels and has been used to generate one year of simulated CarbonSat observations. How this data set has been generated is described in Sect. 5. In Sect. 6, an analysis of the global data is presented. This comprises spatio-temporal averages and assessments for various regions as relevant for the application to quantify natural CO_2 and CH_4 fluxes on regional scales. Limitations of our approach and an outlook to future work are shortly discussed in Sect. 7. A summary and conclusions are given in Sect. 8.

2 CarbonSat mission and instrument concept

CarbonSat aims to deliver the data products XCO_2 (in ppm) and XCH_4 (in ppb) at a high spatial resolution of $2\,\text{km} \times 2\,\text{km}$ and good spatial coverage via continuous imaging across a 240 km swath width (CarbonSat's "breakthrough requirement" rather than the more demanding "goal requirement" of 500 km). The orbit will be sun-synchronous. For this study we assume that the orbit will be similar to NASA's Terra satellite (www.nasa.gov/terra/) but with an Equator-crossing time of 11:30 local time descending node (LTDN).

CarbonSat's main measurement mode will be the nadir (downlooking) mode. CarbonSat will also obtain solar spectra and perform observation in sun-glint mode, especially to improve the quality of the observations over water and snow- and ice-covered land surfaces, which scatter and reflect weakly in the shortwave–infrared (SWIR) spectral region outside of sun-glint conditions. As the sun-glint observation strategy has not yet been finally decided and because the BESD/C retrieval algorithm has not yet been optimized for sun-glint conditions, the CarbonSat sun-glint observations are not considered in this study. Here we focus on nadir mode observations over snow- and ice-free land surfaces.

The CarbonSat imaging spectrometer will cover three spectral bands (Table 1). The near-infrared (NIR) band covers the O_2 A-band spectral region (747–773 nm) at 0.1 nm spectral resolution (approximately $1.7\,\text{cm}^{-1}$). This band yields important information on aerosols, clouds, surface pressure and vegetation chlorophyll fluorescence (VCF). The first SWIR band (SWIR-1) observes the 1590–1675 nm spectral region having a 0.3 nm spectral resolution (approximately $1.2\,\text{cm}^{-1}$). This spectral region contains important weak absorption bands of CO_2 and CH_4 but is otherwise quite transparent (apart from weak water vapour absorption). Thus this provides information on the CO_2 and CH_4 columns with high near-surface sensitivity. The "strong CO_2 band", SWIR-2, measures the 1925–2095 nm spectral region having a spectral resolution of 0.55 nm (approximately $1.4\,\text{cm}^{-1}$). It contains additional information on CO_2 as well as on water vapour and cirrus clouds, the latter from the saturated water band located at 1940 nm. The basic inversion approach is to retrieve CO_2 and CH_4 columns from the transparent SWIR-1 band and to use in addition the partly non-transparent NIR and SWIR-2 bands located at shorter (NIR) and longer (SWIR-2) wavelengths to obtain information on molecular O_2 absorption and atmospheric scatterers at 0.76 μm (NIR) and 2 μm (SWIR-2) in order to constrain the CO_2 and CH_4 retrieval at 1.6 μm (SWIR-1). In practice, all the needed information will be retrieved quasi-simultaneously by applying an appropriate retrieval algorithm to all three bands (see Sect. 3).

For this study we use the latest specification of the CarbonSat imaging spectrometer currently available. Some further optimization of instrument requirements might be possible during mission development. The CarbonSat instrument specification, following an optimization exercise and as used for this study, is similar, but not identical, to that described in Bovensmann et al. (2010). The most relevant differences are that (i) the spectral resolution is somewhat coarser, especially in the NIR and SWIR-2 bands, resulting from a reduction in instrument complexity; (ii) the spectral coverage has been enlarged for the NIR band to include firstly more clear Fraunhofer lines as recommended by Frankenberg et al. (2012), and secondly, for the SWIR-2 band in order to cover a saturated water band at 1940 nm for improved cirrus detection in a manner similar as used for SCIAMACHY

Table 1. CarbonSat instrument spectral parameters as used for this study.

Parameter	Spectral band			Comment
	NIR	SWIR-1	SWIR-2	
Spectral range (nm)	747–773	1590–1675	1925–2095	–
Spectral resolution FWHM (nm)	0.1	0.3	0.55	FWHM is the "full width at half-maximum" of the instrument spectral response function (ISRF).
Spectral sampling ratio (SSR) (1/FWHM)	3	3	3	SSR is the number of spectral elements (detector pixel) per spectral resolution FWHM.
Signal-to-noise ratio (SNR) (–)	150 at 3×10^{12}	160 at 1×10^{12}	130 at 3×10^{11}	SNR (per spectral element) given as SNR_{ref} at L_{ref}, where L_{ref} is a reference radiance value in $[\text{photon s}^{-1} \text{cm}^{-2} \text{nm}^{-1} \text{sr}^{-1}]$. Radiance ($L$) dependence of SNR: $SNR(L) = SNR_{ref} \times \sqrt{L/L_{ref}}$ if $L \geq L_{ref}$ and $SNR(L) = SNR_{ref} \times L/L_{ref}$ if $L < L_{ref}$.

(Heymann et al., 2012b) and GOSAT (Guerlet et al., 2013b); and (iii) the signal-to-noise ratio (SNR) has been enhanced. For this study we use the required threshold (i.e. minimum) SNR performance of CarbonSat (see Table 1) and not, as in Bovensmann et al. (2010), a SNR model.

The instrument parameters (Table 1) are used by a CarbonSat instrument model, which converts high spectral resolution spectra as computed with the radiative transfer model SCIATRAN (Rozanov et al., 2005; Rozanov and Kokhanovsky, 2006; Rozanov et al., 2014) into simulated CarbonSat observations taking into account the relevant instrument characteristics as listed in Table 1. As an example, Fig. 1 shows a simulated CarbonSat nadir radiance spectrum, the solar irradiance, the corresponding sun-normalized radiance and signal-to-noise ratio (SNR) spectra for a scene with vegetation albedo (NIR: 0.2; SWIR-1: 0.1; SWIR-2: 0.05) and a solar zenith angle (SZA) of 50°.

3 BESD/C retrieval algorithm description

For this study the BESD/C retrieval algorithm (Bovensmann et al., 2010) has been used. The acronym BESD stands for "Bremen optimal EStimation DOAS", where DOAS stands for differential optical absorption spectroscopy. BESD/C retrieves XCO_2 and XCH_4 and additional parameters (e.g. for aerosols and cirrus clouds) from a simultaneous analysis of the three CarbonSat bands NIR, SWIR-1 and SWIR-2. BESD/C is described in detail in Bovensmann et al. (2010). Therefore we give here only a short overview focusing on recent improvements.

BESD/C is similar but not exactly identical to the BESD algorithm used for SCIAMACHY XCO_2 retrieval (Reuter et al., 2010, 2011). BESD/C and BESD are "full physics" (FP) retrieval algorithms. As shown in Bovensmann et al. (2010), BESD/C also yields "proxy" (PR) retrievals. BESD/C retrieves CO_2 and CH_4 vertical columns (in

molecules per cm^2), which are converted into dry air column-averaged mole fractions or mixing ratios, i.e. XCO_2 (in ppm) and XCH_4 (in ppb), by dividing the retrieved GHG columns by the dry air column (in number of air molecules, except water vapour, per cm^2). For a FP algorithm, the (dry) air column is obtained from retrieved surface pressure, e.g. obtained from the O_2 A-band spectral region, or from surface pressure obtained from meteorological analysis fields (corrected for water vapour using retrieved or meteorologically analysed water vapour columns). Both sources of information are used to compute the dry air column as the retrieval will use meteorological information as first-guess and a priori information. For a PR algorithm, the air column is obtained from a reference gas, which is CO_2 in the case of PR XCH_4 (e.g. Frankenberg et al., 2005; Schneising et al., 2011; Krings et al., 2013) or CH_4 in the case of PR XCO_2 (see Bovensmann et al., 2010; Krings et al., 2011). The reference gas should be less variable than the target gas (or can be modelled with sufficient accuracy). Typically PR retrievals require a correction procedure for variations of the reference gas using a model (see also Schepers et al. (2012) for a discussion of FP versus PR retrievals). Whether a PR method is appropriate to use depends on the application. In comparison, the FP method is always applicable, as it does not require any assumptions on the reference gas. In this study we focus on FP retrievals and discuss PR retrievals only briefly. Despite the mentioned limitations, PR retrievals have the advantage that systematic errors (caused by, for example, clouds and aerosols) cancel to a large extent when the GHG column ratio is computed (we illustrate this using one example). For some applications (e.g. Bovensmann et al., 2010; Krings et al., 2011, 2013) this is advantageous as it enhances the accuracy.

BESD/C is based on "optimal estimation" (OE) (Rodgers, 2000) and uses a priori information to constrain the retrieval. BESD/C has already been applied to simulated CarbonSat
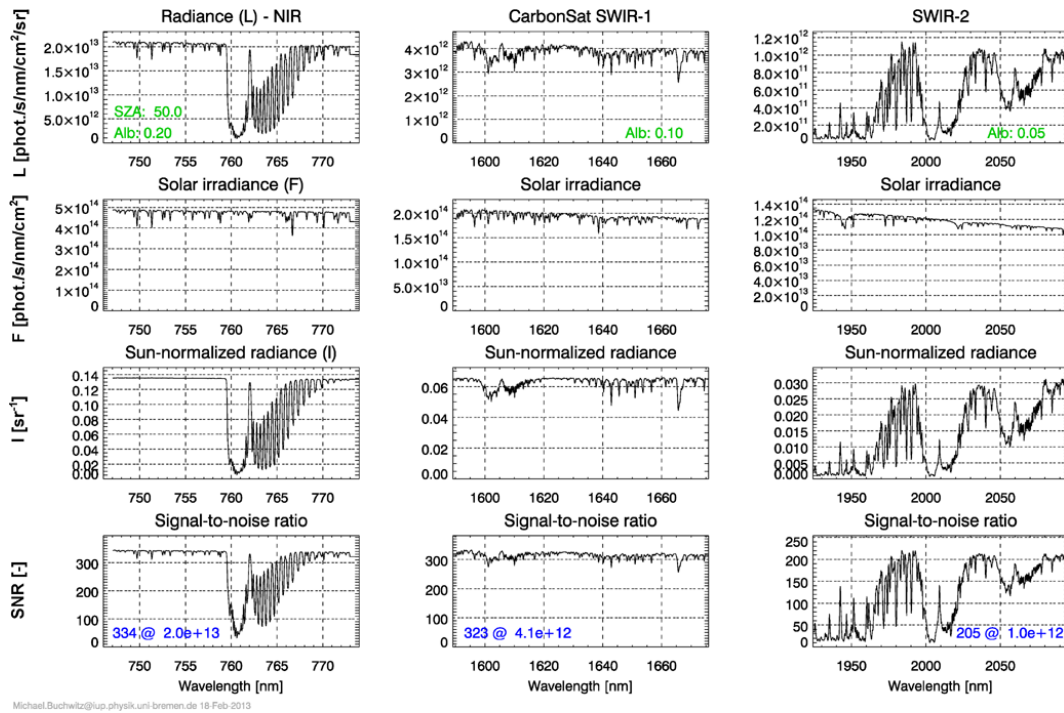
Fig. 1. CarbonSat nadir radiance (top panels), solar irradiance (2nd row), sun-normalized radiance (3rd row) and signal-to-noise ratio (SNR, bottom panels) spectra for vegetation albedo and a solar zenith angle (SZA) of 50° ("VEG50 scenario"). Listed (in green, top row) are the SZA and the albedo ("Alb") in the three bands as well as (in blue, bottom row) the (continuum) SNR and corresponding continuum radiance level.

observations, as shown in Bovensmann et al. (2010). In that publication BESD/C has been used via a fast non-iterative look-up-table approach. For the results presented here, BESD/C has been improved to enhance the accuracy. This has been achieved by fully coupling BESD/C to the radiative transfer model (RTM) SCIATRAN (Rozanov et al., 2005; Rozanov and Kokhanovsky, 2006; Rozanov et al., 2014) as this permits an iterative retrieval by calling the RTM with updated parameters after each iteration step. During the iteration, the BESD cost function (see Eq. 7 in Bovensmann et al., 2010) is minimized. The method used to minimize the cost function is based on the Levenberg–Marquardt algorithm and is identical for BESD and BESD/C and described in Reuter et al. (2011). This (or an equivalent) iterative procedure improves the accuracy of the retrieved XCO_2 and XCH_4 in the presence of variable (and unknown) amounts of aerosols and cirrus clouds and is essentially the standard method also used by other algorithms (e.g. O'Dell et al., 2012; Butz et al., 2011; Reuter et al., 2010, 2011).

Compared to the BESD/C version described in Bovensmann et al. (2010), the BESD/C state vector, which contains all elements to be retrieved via the OE retrieval procedure, has been extended. All state vector elements are listed in Table 2. For each state vector element the derivative of the radiance with respect to the state vector element is needed to characterize the change of the radiance due to a change
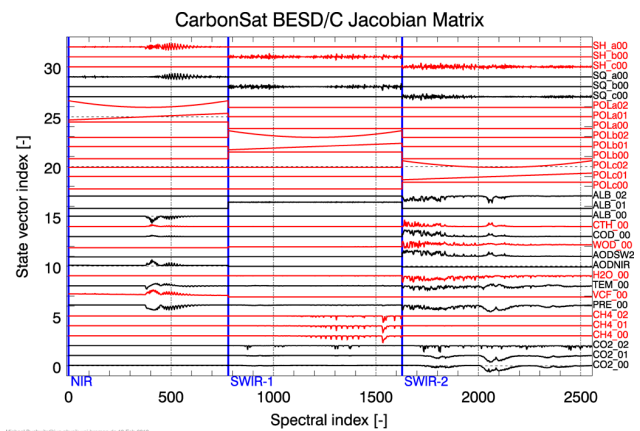

Fig. 2. Typical BESD/C Jacobian matrix. For an explanation of each spectrum (= column of Jacobian matrix), see Table 2.

of that state vector element. These derivatives define the Jacobian matrix, which contains the derivative spectra in each of its columns (for the BESD/C Jacobian matrix, see matrix **K** described in Bovensmann et al., 2010). For BESD/C the derivative spectra are computed (quasi-analytically) by SCIATRAN.

A typical BESD/C Jacobian matrix as used for this study is shown in Fig. 2. Note that each spectrum has been scaled

Table 2. BESD/C state vector elements (default settings). The corresponding spectra (columns) of the Jacobian matrix are shown in Fig. 2. For the retrieval the following three layers are used: lower troposphere (LT, "_00"), upper troposphere (UT, "_01"), stratosphere (ST, "_02").

No.	ID	Explanation	A priori uncertainty
1	SH_a00	Spectral shift parameter NIR band	0.1 nm
2	SH_b00	Spectral shift parameter SWIR-1 band	0.1 nm
3	SH_c00	Spectral shift parameter SWIR-2 band	0.1 nm
4	SQ_a00	Spectral squeeze/stretch parameter NIR band	$0.001\,\mathrm{nm\,nm}^{-1}$
5	SQ_b00	Spectral squeeze/stretch parameter SWIR-1 band	$0.001\,\mathrm{nm\,nm}^{-1}$
6	SQ_c00	Spectral squeeze/stretch parameter SWIR-2 band	$0.001\,\mathrm{nm\,nm}^{-1}$
7	POL_a02	Polynomial coefficient 2 NIR band	1000 (rel.)
8	POL_a01	Polynomial coefficient 1 NIR band	1000 (rel.)
9	POL_a00	Polynomial coefficient 0 NIR band	1000 (rel.)
10	POL_b02	Polynomial coefficient 2 SWIR-1 band	1000 (rel.)
11	POL_b01	Polynomial coefficient 1 SWIR-1 band	1000 (rel.)
12	POL_b00	Polynomial coefficient 0 SWIR-1 band	1000 (rel.)
13	POL_c02	Polynomial coefficient 2 SWIR-2 band	1000 (rel.)
14	POL_c01	Polynomial coefficient 1 SWIR-2 band	1000 (rel.)
15	POL_c00	Polynomial coefficient 0 SWIR-2 band	1000 (rel.)
16	ALB_02	Surface albedo SWIR-2 band	0.05 (rel.(*))
17	ALB_01	Surface albedo SWIR-1 band	0.05 (rel.(*))
18	ALB_00	Surface albedo NIR band	0.05 (rel.(*))
19	CTH_00	Cirrus top height	0.1 (rel.)
20	COD_00	Cirrus optical depth	1.0 (rel.)
21	WOD_00	(Low-lying thin) water cloud optical depth	1.0 (rel.)
22	AOD_SW2	AOD SWIR-2 band	0.5 (rel.)
23	AOD_NIR	AOD NIR band	0.5 (rel.)
24	H2O_00	Scaling parameter for water vapour profile	1.0 (rel.)
25	TEM_00	Shift parameter for temperature profile	0.1 (rel.)
26	VCF_00	Scaling factor for vegetation chlorophyll fluorescence	variable (via DVCF retrieval pre-processing)
27	PRE_00	Surface pressure	
28	CH_4_02	Methane sub-column layer ST	0.001 (rel.)
29	CH_4_01	Methane sub-column layer UT	0.005 (rel.)
30	CH_4_00	Methane sub-column layer LT	0.10 (rel.)
31	CO_2_02	CO_2 sub-column layer ST	0.005 (rel.)
32	CO_2_01	CO_2 sub-column layer UT	0.005 (rel.)
33	CO_2_00	CO_2 sub-column layer LT	0.10 (rel.)

* The a priori surface albedo is obtained via a pre-processing step from the (nearly absorption-free) continuum radiance in each band.

such that the spectra do not overlap in this figure and that it is not possible to see all relevant details in Fig. 2. For example, for AOD retrieval, two Jacobians are shown, namely "AOD-NIR" and "AODSW2". AODNIR covers the NIR and SWIR-1 bands (and is zero in the SWIR-2 band), whereas AODSW2 covers the SWIR-2 and SWIR-1 bands (and is zero in the NIR band). The spectral variations of these two Jacobians in the SWIR-1 band are difficult to see in this figure as the amplitude of these Jacobians is much larger in the two "strongly absorbing" NIR and SWIR-2 bands (in the NIR due to strong O_2 absorption; in the SWIR-2 due to strong CO_2 and H_2O absorption). This indicates that AOD information can primarily be retrieved from the NIR and SWIR-2 bands. The coupling with the SWIR-1 band ensures (at least to some extent) that AOD information obtained from the NIR and SWIR-2 bands is "made available" in the SWIR-1 band.

Recently it has been shown that terrestrial VCF emission needs to be considered for accurate XCO$_2$ retrieval (Frankenberg et al., 2012; Joiner et al., 2011). BESD/C has therefore been improved to consider this. Figure 2 also shows the VCF Jacobian. How the VCF retrieval is performed is explained in Appendix A, together with first simulations indicating that CarbonSat can provide useful information on VCF with a single-measurement precision of approximately $0.3\,\mathrm{mW\,m}^{-2}\,\mathrm{nm}^{-1}\,\mathrm{sr}^{-1}$ (1σ) at 755 nm.

BESD/C as described here has been applied to a number of scenarios to quantify random and systematic XCO$_2$ and XCH$_4$ errors. Results of this exercise are presented and discussed in the following sections.

4 $X\mathrm{CO_2}$ and $X\mathrm{CH_4}$ error analysis and parameterization

In this section we present and discuss our error analysis and error parameterization approach for scattering-related errors. We focus on systematic $X\mathrm{CO_2}$ and $X\mathrm{CH_4}$ retrieval errors but also discuss random errors due to instrument noise. There are several other error sources, such as residual calibration errors, which contribute to systematic (and random or quasi random) errors. These error sources have been considered when formulating the CarbonSat mission and instrument requirements but are not discussed here. The main goal of the error parameterization described here is to compute random and scattering-related systematic errors for each single CarbonSat observation for a one-year time period. Due to the large number of CarbonSat observations, this requires an appropriate (i.e. very fast but sufficiently accurate) scheme to compute these errors. How this has been achieved is described in the following.

4.1 General considerations

Systematic retrieval errors especially for scattering parameters depend significantly on parameters such as the amount of aerosol (characterized by, for example, AOD at the relevant wavelengths), cirrus optical depth (COD), cirrus top height (CTH) and surface spectral reflectance (characterized by, for example, Lambertian surface albedo). A first assessment and analysis of CarbonSat $X\mathrm{CO_2}$ and $X\mathrm{CH_4}$ errors due to aerosols and clouds has already been presented in Bovensmann et al. (2010), focusing on CarbonSat power plant overpasses. Here we present an extension of that analysis to assess the quality of the global data. We aim at estimating random and systematic $X\mathrm{CO_2}$ and $X\mathrm{CH_4}$ errors for one year of CarbonSat global observations. Ideally, this should be done by applying the retrieval algorithm to all individual observations. However, due to the large amounts of data Carbon-Sat will generate, and because the retrieval program BESD/C as currently implemented is quite slow, this is not yet possible. Optimizing the processing time is an important task for the future. For the purpose of this study we have developed an error parameterization scheme, which is described in this section. This scheme permits one to compute the $X\mathrm{CO_2}$ and $X\mathrm{CH_4}$ errors as a function of several scattering-related critical input parameters. A similar approach has also been used by Hungershoefer et al. (2010) to assess the impact of satellite $X\mathrm{CO_2}$ errors for $\mathrm{CO_2}$ surface flux inversions.

The goal of this study is to realistically estimate the expected CarbonSat performance in terms of $X\mathrm{CO_2}$ and $X\mathrm{CH_4}$ random and systematic errors. Random errors are primarily determined by the instrument signal-to-noise performance. It is believed that random errors can be reliably quantified already at this early stage (note that the instrument design is still being optimized) assuming, for example, that detectors will not dramatically improve in the near future. Systematic

errors, however, also critically depend on the retrieval algorithm and its parameter settings. It is expected that the BESD/C algorithm will be significantly further improved in the coming years, e.g. by better exploiting the strong water band in the 1940 nm spectral region for cirrus detection (e.g. Heymann et al., 2012b), by further improving the aerosol retrieval method by also retrieving an aerosol size parameter (e.g. Butz et al., 2011) or by taking advantage of existing scattering-related global data sets to improve the a priori information on aerosols and cirrus. One way to consider future improvements could be to reduce systematic errors by a certain factor. Such a factor cannot, however, be reliably estimated. For this study we use BESD/C as is. However, we solve a somewhat simplified retrieval problem, e.g. by focusing only on a few parameters, which are known to be critical ones. Our approach is more advanced than the relatively simple approach for other dedicated GHG satellite missions as used by Hungershoefer et al. (2010) as we consider more parameters, but it is still quite simple as we neglect, for example, microphysical parameter variations for aerosols (this aspect is further discussed in Sect. 7).

Another question is which a priori information is, for example, required for scattering-related and other parameters. A future operational CarbonSat algorithm will very likely use a priori information for several parameters as this will reduce systematic GHG retrieval errors. This is also the approach used by the operational GOSAT algorithm (Yoshida et al., 2011, 2013). Here we utilize the following simple approach. We use constant a priori values for COD (0.05), CTH (10 km) and AOD (0.2 at 550 nm, corresponding to 0.117 at 760 nm for "continental average" aerosol; see Sect. 7), but to compensate for this, we assume good knowledge of the surface albedo by using the true albedo, i.e. the one used to generate the simulated observations, in each band as first-guess value. Note that BESD/C retrieves surface albedo (see ALB state vector elements listed in Table 2) and first-guess values are obtained using a pre-processing scheme based on transparent spectral regions as located in each of the three bands. Nevertheless, systematic $X\mathrm{CO_2}$ and $X\mathrm{CH_4}$ retrieval errors are reduced if surface albedo is well known, especially for low albedo scenes, where aerosols and cirrus may significantly influence the backscattered radiance reaching the top of the atmosphere.

4.2 Error analysis based on individual BESD/C retrieval

For the error analysis (and the error parameterization; see following section) a number of scenarios have been defined using different combinations of COD, CTH, AOD, surface albedo and SZA; these are shown in Fig. 3. For each scenario, high-spectral-resolution radiance spectra have been computed with SCIATRAN and converted to simulated CarbonSat spectral observations using the CarbonSat instrument model mentioned in Sect. 2. BESD/C has been applied to
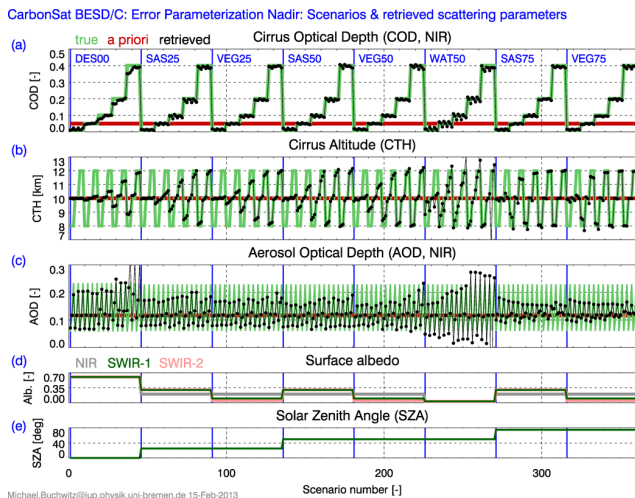
Fig. 3. Scenarios defined for the error parameterization and corresponding retrieval results. **(a)** Shows the model atmosphere cirrus optical depth (COD) as green line for all 360 scenarios. The red line shows the a priori COD as used for BESD/C retrieval. The retrieved COD is shown as a black line and black dots. Also listed are the scenario identifiers indicating surface albedo – DES = desert, SAS = sand/soil, VEG = vegetation, WAT = water (see **(d)**) – and solar zenith angle (SZA), 00 = 0°, 25 = 25°, etc. (see **(e)**). **(b)**, same as **(a)** but for cirrus altitude (cloud top height – CTH). **(c)**, same as **(a)** but for aerosol optical depth (AOD) at 765 nm (NIR band).

each simulated observation to retrieve XCO$_2$ and XCH$_4$ and to determine their errors.

Random errors depend primarily on the signal-to-noise performance of the instrument. The OE retrieval method permits one to map this error from radiance space to state vector (i.e. retrieval parameter) space. The random error of the spectra have been computed using signal-to-noise ratio computations, as described in Sect. 2. Note that the noise has not been added to the spectra. Instead, the random error spectra ("measurement error") have been used as input for the OE method. The random errors of the state vector elements have been computed from the diagonal elements of the state vector variance–covariance matrix, which is an output of the OE retrieval method in addition to other parameters such as the retrieved state vector itself (see Bovensmann et al. (2010) and Rodgers (2000), where all relevant formulas are given).

Systematic XCO$_2$ and XCH$_4$ errors are computed as "retrieved minus true", where the true values are the known values from the model atmosphere used to generate the simulated observations. As described above, we use constant values as a priori and initial values for the retrieval for AOD and COD and cirrus altitude. For the simulated observations we use different values of these and other parameters but still assume the same physical treatment of scattering processes for the retrievals. Systematic XCO$_2$ and XCH$_4$ errors originate from the fact that the iterative retrieval method does typically not find the true solution for all parameters. This is because

of the non-linear nature of the retrieval problem and correlations between state vector elements. Due to the fact that many parameters are correlated at least to some extent, e.g. CO$_2$ and cirrus (see Jacobians shown in Fig. 2), a systematic cirrus error can, for example, lead to a systematic XCO$_2$ error.

After BESD/C retrieval, a quality flag is set, which depends on the retrieved scattering parameters. Here we only flag those retrievals as "good" for which the sum of the retrieved AOD (at NIR wavelength) and COD is less than 0.3 (i.e. AOD(NIR) + COD < 0.3). This filtering criterion is similar as used, for example, for GOSAT XCO$_2$ retrieval (Guerlet et al., 2013b; O'Dell et al., 2012). Applying such a criterion requires that COD and AOD (or, strictly speaking, their sum) can be retrieved with sufficient accuracy.

As shown in Fig. 3a, COD can be retrieved very well. This is shown by the typically very good agreement between retrieved COD (black dots) and true COD (green line). The retrieved AOD correlates with the true values but the absolute retrieved values are not perfect; typically the full variability is not captured by the retrieval. This shows that COD can be retrieved with higher accuracy than AOD. The reason for this is that the AOD changes are primarily due to changes of the aerosol amount in the boundary layer, which has less impact on the radiance than COD changes in the upper troposphere. As can also be seen in Fig. 3b, CTH can also be retrieved quite well at least if COD is not too low. Note that for this error analysis, as already explained, we only study very thin clouds as it is assumed that all ground pixels with significant cloud contamination have already been identified and removed (see also Sect. 5).

Figure 4 shows the corresponding XCO$_2$ and XCH$_4$ random and systematic errors for the same scenarios as shown in Fig. 3. The results for all scenarios are shown as a light red line, and the quality-filtered, i.e. "good", retrievals are shown as red diamonds. Figure 5 is a close-up of Fig. 4 to show more details for all those scenarios, which correspond to a SZA of 50°.

As can be seen, the XCO$_2$ random error is typically around 1 ppm except for low surface albedo (see WAT50 scenarios in Figs. 4 and 5 corresponding to a water albedo of 0.03 in all spectral bands and a SZA of 50°), where the precision is close to 2 ppm, and for some high SZA scenarios (VEG75, i.e. vegetation albedo and SZA 75°, as shown in Fig. 4), where the XCO$_2$ precision exceeds 2 ppm for high COD. The XCH$_4$ random error has a similar scenario dependence. It is typically between 5 and 10 ppb except for the WAT50 and VEG75 scenarios, where it is typically between 15 and 20 ppb or even larger for VEG75 if COD is high.

The systematic errors are more complex as they depend more strongly on the scenario, especially for low-albedo (WAT50) and high-SZA (75°) scenarios (e.g. SAS75, corresponding to sand/soil albedo, and VEG75). For the "less extreme" albedo and SZA scenarios (i.e. DES00, where DES is desert albedo, SAS25, VEG20, SAS50, and VEG50) the
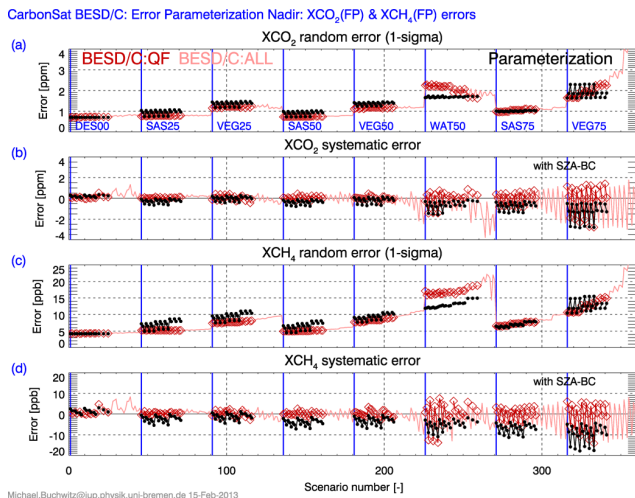
Fig. 4. BESD/C retrieval and error parameterization results. Shown are the unfiltered BESD/C results for all 360 scenarios (see Fig. 3) as a light red solid line. The quality-filtered BESD/C results are shown as red diamonds. The filtered results correspond to those retrievals where the retrieved AOD(NIR) + COD < 0.3. To model the quality-filtered BESD/C results, an error parameterization scheme has been developed and the corresponding results are shown in black. Results are shown for the following parameters: **(a)** XCO$_2$ random error, **(b)** XCO$_2$ systematic error, **(c)** XCH$_4$ random error and **(d)** XCH$_4$ systematic error.
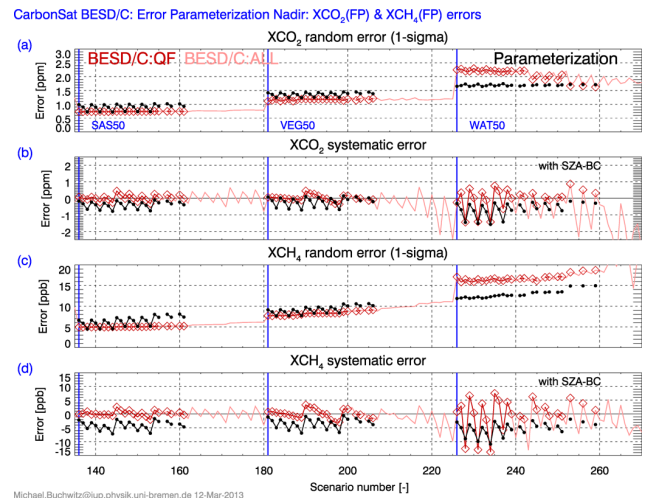

Fig. 5. Close-up of Fig. 4 (using the same colour scheme as used for Fig. 4) for the three SZA 50° scenarios corresponding to surface albedos sand/soil (SAS), vegetation (VEG) and water (WAT). As can be seen, the error parameterization tends to overestimate random errors except for very low albedo scenes (WAT), where the random errors are typically underestimated. As can also be seen, the error parameterization tends to produce a low bias (too negative systematic error), especially for the SAS and VEG albedo scenes, and does not capture the full variability of the biases for very low albedo scenes (WAT).

systematic XCO$_2$ error is a few tenths of a ppm and the systematic XCH$_4$ error is a few ppb. For the "more extreme" scenarios WAT50, SAS75 and VEG75, the systematic error can be much larger, up to about 3 ppm for XCO$_2$ and nearly 20 ppb for XCH$_4$. Also the dependence on cirrus OD, cirrus altitude and AOD is much larger for these scenarios. Because low albedos such as water (or snow and ice in the SWIR bands) result in large errors, we focus in this manuscript on (snow- and ice-free) land surfaces. Exploitation of the CarbonSat sun-glint observations will provide improved the signal-to-noise ratio and therefore the sensitivity for the retrieval of XCO$_2$ and XCH$_4$ over water scenes, but a discussion of this is out of the scope of this study. The large variation of the errors at high SZA is also a potential issue, requiring optimization. Therefore we limit the further analysis as presented in Sect. 5 and following sections to a maximum SZA of 70°.

4.3 Error parameterization

In order to generate one year of simulated CarbonSat observations we have developed an error parameterization scheme to parameterize the XCO$_2$ and XCH$_4$ random and systematic errors and their averaging kernels (which describe the change of the retrieved quantity, e.g. XCO$_2$, resulting from a change of the true quantity caused by a perturbation at a given altitude (e.g. the perturbation of the CO$_2$ mixing ratio)). For

this purpose we defined a number of regression functions and applied a linear regression scheme to the quality-filtered, i.e. "good", retrievals, as shown in Figs. 4 and 5 (red diamonds) and already discussed in the previous section.

Linear regression has been used to parameterize the XCO$_2$ and XCH$_4$ random and systematic errors (four quantities) and their averaging kernels. The averaging kernels (AK) as a function of pressure level (p, used as vertical coordinate), AK(p), are approximated by a low-order polynomial defined by the three polynomial coefficients P0, P1 and P2 such that AK $(p) = $ P0 $+$ P1 $\cdot p/p_\circ +$ P2 $\cdot (p/p_\circ)^2$, where $p_\circ$ is surface pressure. Three coefficients are used for the XCO$_2$ AK and three for the XCH$_4$ AK. In total 10 quantities have been parameterized.

The regression function used for the parameterization of each parameterized quantity Q is

$$Q = \sum_{i=0}^{7} C_i X_i. \qquad (1)$$

Here Q is any of the 10 to-be-parameterized quantities and X_i is the ith regression function and C_i the corresponding regression coefficient. The regression functions are identical for all 10 quantities but the regression coefficients differ for each quantity. The regression functions are listed in Table 3 and the corresponding coefficients in Table 4. Regression function X_0 is a constant (offset). Each of the regression functions $X_1–X_7$ correspond to one of the six key

Table 3. Error parameterization regression functions X0–X7. "Valid range" indicates the approximate range of values for which the parameterization is valid.

Function	Definition	Explanation	Valid range
X0	1.0	Constant offset	
X1	SZA – 50.0	SZA in [deg]	0–80
X2	ALBN – 0.1	Albedo NIR band [–]	0.03–0.7
X3	ALBS – 0.1	Albedo SWIR-1 band [–]	0.03–0.7
X4	AOD – 0.2	Aerosol optical depth at 550 nm [–]	0–0.6
X5	COD – 0.05	Cirrus optical depth (NIR) [–]	0–0.6
X6	CTH – 10.0	Cirrus top height [km]	2–20
X7	AOD · INC_SZA · INC_ALB	where	
		AOD as for X4 and	
		INC_SZA = cos(84)/cos(SZA+9) · SZA/75	
		INC_ALB = (1.01/(ALBS+0.01)−1) · 0.01	

inputs parameters (e.g. SZA, NIR albedo) or a combination of them (X_7) as listed in Table 3. Table 3 also lists the valid range of these input parameters (for example, the regression should not be used for SZA larger than about 80°).

After computation of Q according to Eq. (1), some further computations are needed to compute the final values of the XCO_2 and XCH_4 random and systematic errors. Random errors: if the XCO_2 or XCH_4 random errors are less than (the pre-defined minimum value of) 0.7 ppm for XCO_2 and 4.2 ppb for XCH_4, the corresponding values should be set to these minimum values. This avoids unrealistically small (or even negative) random errors. Systematic errors: for the XCO_2 and XCH_4 systematic errors a "SZA bias correction" should be applied as follows: for XCO_2 the term SZA/70-0.2 should be subtracted, and for XCH_4 the term $8.0 \times$ SZA/70.0-1.0. Without this correction the global bias maps (e.g. Fig. 9b and d) would show an obvious SZA dependent bias at high SZA, which could very likely be identified and corrected for when analysing real CarbonSat data. More advanced bias correction schemes such as the ones currently used, for instance, for real GOSAT data (e.g. Crisp et al., 2012; Cogan et al., 2012) are, however, not used in this study.

The error parameterization results for the XCO_2 and XCH_4 errors are shown in Figs. 4 and 5 (black dots). The error parameterization computes the desired output parameters based on six input parameters. The input parameters are the parameters which define the scenarios shown in Fig. 3, i.e. SZA, albedo in the NIR and SWIR-1 bands, COD, CTH and AOD (at 550 nm). These parameters are assumed to be the six most critical ones. Note that the errors also depend on other parameters not explicitly considered here. One example is SWIR-2 albedo. SWIR-2 albedo variations have been considered for the retrieval simulations but not for the error parameterization. We assume here that the SWIR-1 and SWIR-2 albedos are sufficiently well correlated.

As can be seen from Figs. 4 and 5, the errors computed with the error parameterization method (black dots) capture

the variability of the "real errors" (red diamonds) reasonably well. Poorer agreement is obtained for very low surface albedos (WAT50 scenarios) and for scenarios where the SZA is large, i.e. the SAS75 and VEG75 scenarios. Figure 5, which is a close-up of Fig. 4, shows more details for the scenarios corresponding to an SZA of 50°. As can be seen most clearly in Fig. 4, the error parameterization tends to overestimate the random and systematic errors for typical land surfaces and tends to underestimate the errors for retrievals over water (i.e. for very low albedo scenes). As the focus of this manuscript is on observations over land, the error parameterization results are quite conservative as they tend to overestimate the random and systematic errors as computed using full BESD/C retrievals. In this context it shall be mentioned that also other error parameterization schemes have been investigated based on tabulating the errors obtained by BESD/C retrievals combined with a multi-dimensional interpolation scheme. The agreement of the results obtained with this scheme was, however, poorer than that for the scheme used here, especially for systematic errors, which exhibit complex dependencies on the various input parameters. The main reason why the table-based interpolation scheme did not work well is because of problems related to the quality flagging, which essentially does not permit the generation of a table which is based on a regular grid of input parameters.

The regression scheme also permits one to parameterize the XCO_2 and XCH_4 averaging kernels. The corresponding results are shown in Fig. 6. Shown are "real" (red diamonds) and parameterized (black dots) averaging kernel values at the surface (panels a and b) and at $p/p_o = 0.5$ (panels c and d), where p is the pressure level and p_o denotes surface pressure. As can be seen, the averaging kernels are nearly ideal, i.e. close to 1.0 at the surface for XCO_2 and XCH_4.

In the following section it is described how the error parameterization has been used to generate one year of simulated global CarbonSat observations.

Table 4. Error parameterization regression coefficients C0–C7 for the regression functions listed in Table 3, each corresponding to one of the 10 parameterized quantities Q. Row CO_2_RE (CH_4_RE) contains the coefficients for the XCO_2 (XCH_4) random error. Row CO_2_SE (CH_4_SE) contains the coefficients for the XCO_2 (XCH_4) systematic error. Rows $AK\_CO_2\_P0$ to $AK\_CO_2\_P2$ list the coefficients for the XCO_2 averaging kernel polynomial coefficients P0, P1 and P2. Rows $AK\_CH_4\_P0$ to $AK\_CH_4\_P2$ list the coefficients for the XCH_4 averaging kernel polynomial coefficients P0, P1 and P2.

Q	C0	C1	C2	C3	C4	C5	C6	C7
CO_2_RE	1.29121	−0.00220	−0.07275	−1.97335	−1.00620	0.34586	−0.00150	38.86071
CO_2_SE	0.30786	0.01191	1.97716	−1.55154	−1.40282	0.70400	−0.03020	−73.46152
CH_4_RE	9.47532	−0.02678	−7.84754	−11.52154	−7.88635	15.80352	0.01702	275.25335
CH_4_SE	1.41086	0.05545	9.17830	−6.77504	−9.15046	5.52796	−0.48784	−335.04555
$AK\_CO_2\_P0$	0.25206	−0.00660	−0.97822	1.37264	−0.01718	−0.47370	−0.00132	2.50772
$AK\_CO_2\_P1$	1.34678	0.01515	3.96544	−4.98547	0.32270	0.24450	−0.00951	−15.62410
$AK\_CO_2\_P2$	−0.60245	−0.00851	−2.98224	3.62314	−0.29681	0.22898	0.01084	12.78807
$AK\_CH_4\_P0$	0.93580	−0.01024	−0.68970	−0.13586	0.03922	1.10047	0.00156	−1.59493
$AK\_CH_4\_P1$	−0.13742	0.02801	1.88213	0.18662	−0.20388	−2.84238	−0.01870	11.16231
$AK\_CH_4\_P2$	0.18796	−0.01763	−1.15321	−0.03191	0.19001	1.68905	0.01708	−10.43191

5 Generation of simulated global CarbonSat observations

To generate a data set useful for global inversion studies at regional-scale resolution (e.g. Basu et al., 2013) and other applications (e.g. to derive emissions of cities; Buchwitz et al., 2013b) and to obtain statistical results for different regions (see Sect. 6), a one-year global data set of simulated Carbon-Sat observations has been generated. This data set ("Level 2 error" – L2e – files) contains for each single CarbonSat observation the time and location of the measurement (for the reference year 2008), the relevant angles (e.g. solar and viewing zenith and azimuth angles) and various geophysical parameters such as AOD, COD and CTH. The files contain neither the XCO_2 and XCH_4 errors nor the averaging kernels. Instead, these files contain all the needed information (for each ground pixel) to compute the corresponding values using the error parameterization method discussed in the previous section. The files also do not contain absolute XCO_2 and the XCH_4 values. These values are expected to come from a (global or regional) model as used for the analysis of the CarbonSat data. The model data are expected to be "perturbed", using the provided error characteristics (and averaging kernels) to generate appropriate simulated observations consistent with the model used.

The L2e files have been generated assuming an orbit similar as NASA's Terra satellite (sun-synchronous, descending, Equator-crossing time 10:30 LTDN; see www.nasa.gov/terra/) except for the equator crossing time, which is assumed to be 11:30 LTDN for CarbonSat, i.e. one hour later than Terra. One year of Terra data (year 2008) has been used to generate the L2e files. Geolocation information available in the Terra files has been used for the L2e files. The time information and related quantities, e.g. SZA, have been adjusted to consider the different equator overpass times.
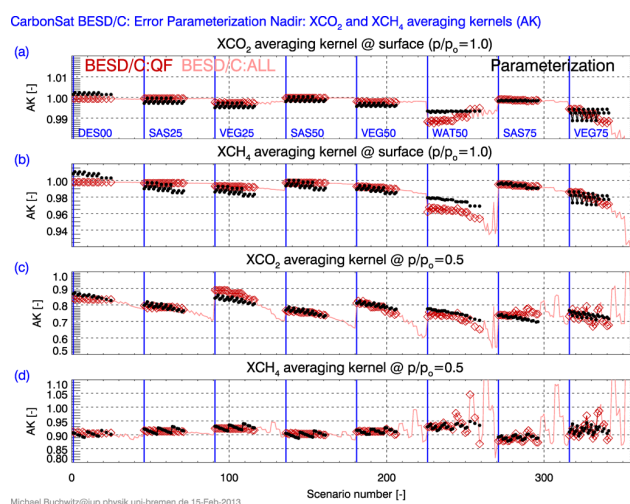

Fig. 6. As Fig. 4 but for the XCO_2 and XCH_4 averaging kernels at $p/p_\circ = 1.0$ (**a** and **b**) and $p/p_\circ = 0.5$ (**c** and **d**), where p is the pressure level (altitude) and $p_\circ$ is surface pressure.

The Moderate Resolution Imaging Spectroradiometer (MODIS) Terra MOD35 data product (http://modis-atmos.gsfc.nasa.gov/MOD35_L2/) with a spatial resolution of about $1\,km \times 1\,km$ has been used to identify and filter out cloud-contaminated CarbonSat ground pixels. Only those ($2\,km \times 2\,km$) CarbonSat ground pixels are classified as cloud-free when all four ($1\,km \times 1\,km$) MODIS pixels located in a given CarbonSat ground pixel ($2\,km \times 2\,km$) are cloud free. The L2e files only contain the cloud-free CarbonSat data as determined using the described procedure. Nevertheless, it can be expected that some cloud contamination remains, in particular thin (sub-visual) cirrus clouds. In order to obtain the cirrus parameters COD and CTH, a "climatology" has been generated using CALIPSO (Winkler et al., 2009). The used CALIPSO (Cloud-Aerosol

Lidar and Infrared Pathfinder Satellite Observations) data product (CAL LID L2 05kmCLay-Prov-V3-01, https:// eosweb.larc.nasa.gov/project/calipso/calipso_table) provides information on COD with a horizontal resolution of 5 km along-track by 70 m across-track. This data product has been processed as described in Heymann et al. (2012a). The CALIPSO data set provides binary information about cloud coverage. Consequently, the relative frequency of cloud occurrence has been computed for every grid box and is used as cloud fractional coverage (CFC) data set. Using CALIPSO-derived COD and CFC, "effective COD" – eCOD ($= \text{COD} \times \text{CFC}$) – has been computed. The (sparse) CALIPSO eCOD and CTH data sets have been spatio-temporally smoothed with a Hann window with an effective width of $8° \times 8°$ and three months, i.e. the cirrus data sets used for this study are at much lower spatio-temporal resolution than the CarbonSat observations.

For aerosols the "GEMS aerosol product" (obtained from http://data-portal.ecmwf.int/data/d/gemsreanalysis/; GEMS: Global and regional Earth-system (Atmosphere) Monitoring using Satellite and in-situ data), as described and used in Heymann et al. (2012a), has been utilized. This data product is based on the assimilation of MODIS data. The time resolution is 12-hourly and the spatial grid is $1.125° \times 1.125°$. For this study primarily the AOD at 550 nm has been used.

For surface albedo, NASA's filled surface albedo data product has been used. This product is based on a climatology (2000–2004) of MODIS MOD43B3 data (http:// modis-atmos.gsfc.nasa.gov/ALBEDO/index.html). This climatology removes snow-covered pixels, which is not a problem for this study as we limit the analysis to snow- and ice-free land surfaces. For the NIR band we use the MODIS albedo at 860 nm.

A number of other parameters are also stored in the L2e files. One example is near-surface wind speed (from the ERA-Interim data set obtained from ECMWF – European Centre for Medium-Range Weather Forecasting). This parameter is relevant, for example, for the analysis of sunglint observations over water. It is, however, not used for this study, which focuses on non-glint observations over land surfaces. Using these input parameters (all stored in the L2e files) and the error parameterization scheme, the $X\text{CO}_2$ and $X\text{CH}_4$ errors have been computed for each single CarbonSat ground pixel.

Figure 7 illustrates this by showing the GHG errors as computed using the error parameterization scheme described above for a single CarbonSat overpass over Germany. Figure 8 shows several other parameters for the same overpass, which are used as input parameters for the error parameterization scheme: albedo, AOD, COD and CTH. The assumed swath width is 500 km (CarbonSat's goal swath width) corresponding to (at maximum, if all cloud-free) 250 across-track ground pixels of size $2 \text{ km} \times 2 \text{ km}$. Gaps are due to thick clouds and additional quality filtering: only those pixels for which the following conditions are all simultaneously met

are classified "good" (simulated retrievals have shown that the quality of the retrievals is low if these conditions are not met):

– Cloud-free (i.e. no thick clouds; see above),

– SZA $< 70°$,

– Albedo(NIR) > 0.05,

– Albedo(SWIR-1) > 0.05,

– Albedo(NIR)/Albedo(SWIR-1) < 4, and

– AOD(550 nm) + COD < 0.4 (approximately equivalent to AOD(NIR) + COD < 0.3 (see Sect. 4) assuming a wavelength dependence of the aerosol extinction inversely proportional to wavelength).

As can be seen, the $X\text{CO}_2$ random error (i.e. the 1-σ single-measurement precision) is close to 1.2 ppm (Fig. 7a) with only some variations correlated with SWIR-1 albedo (Fig. 8a), as expected. This is also true for the $X\text{CH}_4$ random error (Fig. 7c), which is close to 7 ppb. The $X\text{CO}_2$ systematic error (Fig. 7b) typically differs from zero and is about 0.3 ppm on average. Variations around the mean value of 0.3 ppm in the range ±0.3 ppm are also correlated with albedo (Fig. 8a), but likely also to some extent with AOD (Fig. 8b), COD (Fig. 8c) and CTH (Fig. 8d), although this is not so obvious as these correlations are quite low. Note that the spatial fine structure of all errors is primarily due to surface albedo variations (in the NIR and SWIR bands) but not due to aerosols and cirrus, as these data sets were only available at quite low resolution (especially for cirrus), as already explained. This is assumed to be appropriate for regional-scale inversion studies (assuming that essentially only the "average error" matters) but not necessarily for "point sources" such as power plants (e.g. Bovensmann et al., 2010; Krings et al., 2011) or cities (e.g. Kort et al., 2012; Schneising et al., 2013a; Buchwitz et al., 2013b).

As can be seen from Fig. 7, the $X\text{CO}_2$ and $X\text{CH}_4$ errors are highly correlated, as both gases suffer from the same underlying error sources (either instrument noise or systematic scattering-related errors). The results shown in Fig. 7 are based on BESD/C FP retrievals. To a good approximation the data shown in Fig. 7 can be used to estimate the corresponding errors for "proxy" (PR) retrievals. As explained above, PR retrievals are essentially based on computing the column-averaged mixing ratio of the gas of interest by dividing its retrieved column by the retrieved column of a reference gas plus a correction for variations of the reference gas, which is typically done using a model. The application of this method typically requires that the variations of the reference gas are much less than the variations of the target gas. Whether a PR data product can be used or not therefore depends on the application. PR retrievals typically suffer much less from scattering-related errors due to cancellation of errors when computing the ratio. However, their noise (random
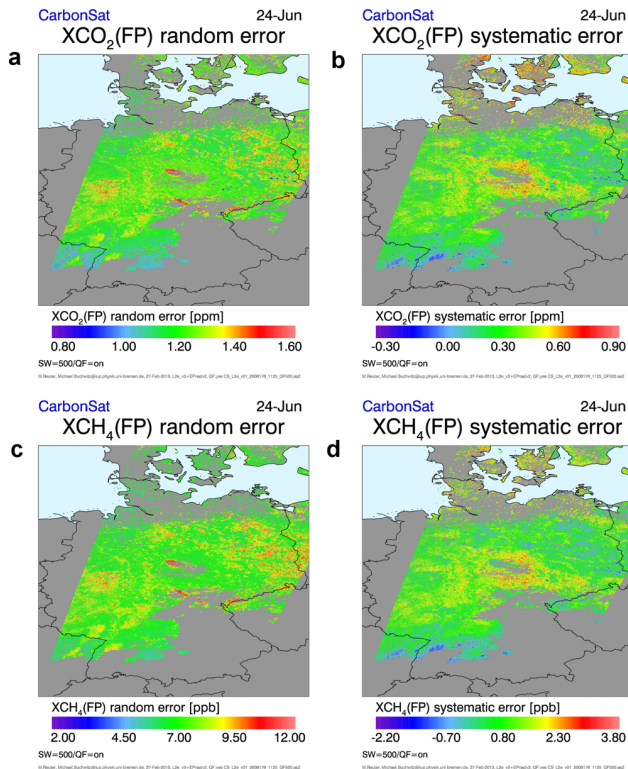
Fig. 7. XCO_2 and XCH_4 random (**a** and **c**) and systematic (**b** and **d**) retrieval errors for a single satellite overpass over Germany assuming a swath width of 500 km. Gaps are due to the limited swath width, (thick) clouds and other filtering criteria, as explained in the main text. The errors have been computed using the error parameterization scheme. Some of the input data which have been used for computing these errors are shown in Fig. 8.

Fig. 8. As Fig. 7 but for the following parameters: **(a)** surface albedo in the SWIR-1 band, **(b)** AOD in the NIR band, and the cirrus parameters COD **(c)** and CTH **(d)**.

error) is typically larger than for FP retrievals due to calculating the ratio of two noisy quantities. Results for PR retrievals are presented and discussed in Appendix B, where it is shown for the scene investigated that the scattering-related systematic XCO_2 and XCH_4 errors of the PR method are typically four times smaller than for FP retrievals. For random errors the opposite is true: the PR random errors are about 83 % larger for XCO_2 and about 28 % larger for XCH_4.

In the following section, the entire one-year global data set is presented and discussed.

6 Analysis of global data

The CarbonSat observations will also be used to quantify CO_2 and CH_4 fluxes globally at regional-scale spatial resolution and approximately monthly time resolution. In this section we present an overview about the global data. We discuss spatio-temporal averages of the XCO_2 and XCH_4 random and systematic errors, obtained from averaging the data contained in the L2e files, and also present detailed results for selected regions.

Figure 9 shows spatio-temporally averaged errors for July for a spatial grid of $5° \times 5°$ (the corresponding figure for January is shown in Appendix C: Fig. C1). As can be seen, the mean XCO_2 random error (panel a) is typically close to 1.1 ppm, except for highly reflecting surfaces such as the Sahara, where the mean precision is in the range 0.5–0.8 ppm (simple direct average, i.e. not divided by the square root of the number of observations or equivalent). The mean systematic XCO_2 error (panel b) is typically within ± 0.3 ppm but may reach or even exceed 0.4 ppm (positive and negative biases). The mean XCH_4 random error (panel c) is typically close to 7 ppb, except for highly reflecting surfaces such as the Sahara, where the mean precision is as low as approximately 4 ppb. The mean systematic XCH_4 error (panel d) is typically within ± 2 ppb but also reaches approximately -4 ppb over large parts of central Africa. The number of observations is large, as shown in Fig. 10. Depending on the month, the number of quality-filtered observations over snow- and ice-free land surfaces is in the range of 33–46 million per month. As described, the random and systematic errors are caused by and depend on critical parameters which have been used as input for the error parameterization scheme. For comparison with Fig. 9, these input parameters are shown in Fig. 11.
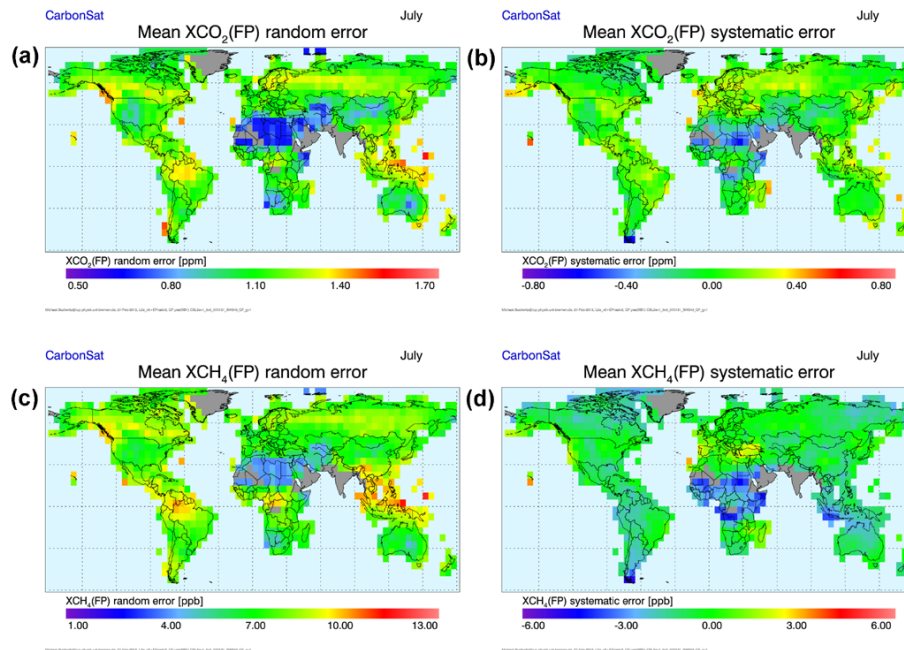
Fig. 9. Spatially averaged ($5° \times 5°$) errors for July for a swath width of 240 km. For this figure all quality-filtered cloud-free observations over snow- and ice-free land surfaces have been averaged.

Finally, we present detailed results for selected regions, which are listed in Table 5. For each of these regions, cumulative error distributions have been computed, as shown in Figs. 12 and 13 and summarized in Table 5. As can be seen, systematic errors are mostly (approximately 85 %) below 0.3 ppm for XCO$_2$ (< 0.5 ppm: 99.5 %) and below 2 ppb for XCH$_4$ (< 4 ppb: 99.3 %). This finding together with the high single-measurement precision and the large amounts of data to be expected from CarbonSat indicates that CarbonSat will be able to make significant contributions for improving our knowledge on the sources and sinks of these two very important GHGs.

7   Limitations and the perspective for future research

The error parameterization scheme permits one to compute random and systematic scattering-related XCO$_2$ and XCH$_4$ errors for the six input parameters solar zenith angle, surface albedo in two bands, AOD and COD, and cirrus altitude. As already pointed out, this scheme is more complex that previously used error parameterization schemes developed for other satellite missions (e.g. Hungershoefer et al., 2010) but is still quite simple. For example, aerosol type variations are neglected and it is assumed that aerosol variability is confined to the boundary layer (here the lowest 2 km of the atmosphere).

For the error parameterization the aerosol type "continental average" (CA) from OPAC (Optical Properties of Aerosols and Clouds) (Hess et al., 1998) is used as
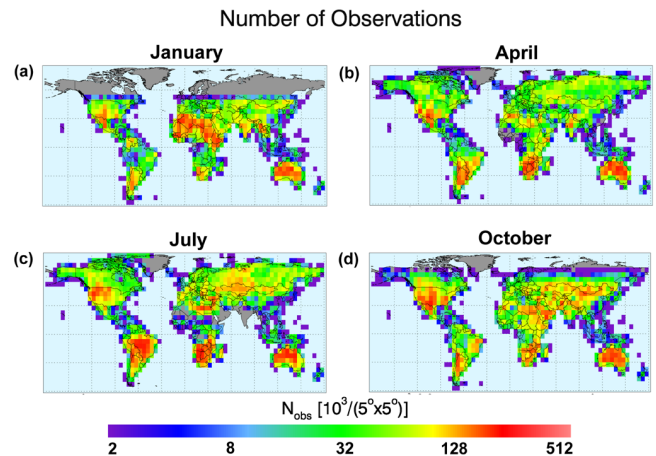

Fig. 10. Number of quality-filtered CarbonSat observations over snow- and ice-free land surfaces for January **(a)**, April **(b)**, July **(c)** and October **(d)** within each $5° \times 5°$ grid cell for a swath width of 240 km in units of 1000 observations per grid cell. The total number of observations per month is 33.15×10^6 for January, 40.40×10^6 for April, 46.28×10^6 for July, and 43.24×10^6 for October.

implemented in the radiative transfer model SCIATRAN (Rozanov and Kokhanovsky, 2006; Kauss, 1998). This aerosol type consists of a mixture of three components: "soot" (fraction: 0.541987), "water soluble" (0.457987), and "dust-like" (0.000026). While for observations over land this is assumed to be a reasonable choice for "average conditions", this does not cover, for example, more polluted
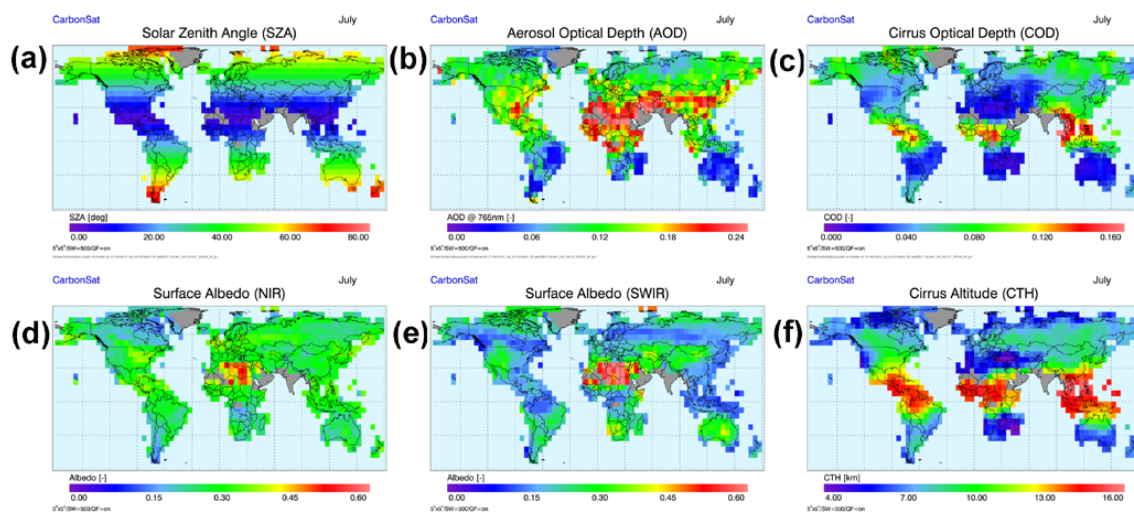
Fig. 11. As Fig. 9 but for the parameters SZA **(a)**, AOD in the NIR band **(b)**, COD **(c)**, surface albedo in the NIR band **(d)**, surface albedo in the SWIR-1 band **(e)** and CTH **(f)**.
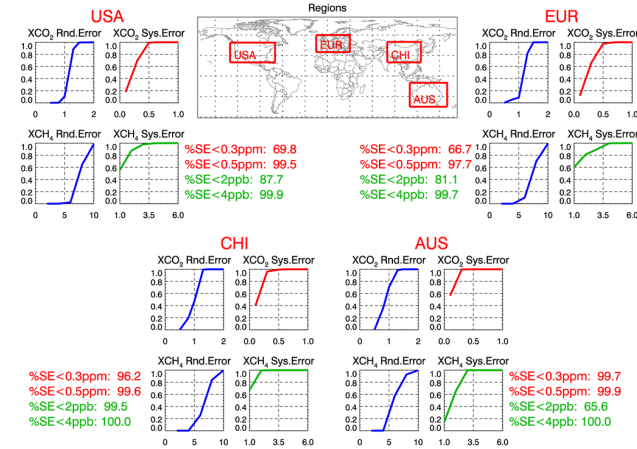
Table 5. Regional cumulative error distribution results summarizing the percentages of errors less than a given value as shown in Figs. 12 and 13.

Region ID	Region name	Latitude (deg)	Longitude (deg)	Percentage of XCO$_2$ retrievals with systematic error < 0.3 ppm	< 0.5 ppm	Percentage of XCH$_4$ retrievals with systematic error < 2 ppb	< 4 ppb
USA	USA	20 °N–49 °N	130 °W–70 °W	69.8	99.5	87.7	99.9
EUR	Europe	35 °N–60 °N	15 °W–30 °E	66.7	97.7	81.1	99.7
CHI	China	20 °N–50 °N	80 °E–125 °E	96.2	99.6	99.5	100.0
AUS	Australia	45 °S–10 °S	110 °E–160 °E	99.7	99.9	65.6	100.0
CAN	Canada	49 °N–70 °N	140 °W–50 °W	97.9	100.0	78.3	100.0
SIB	Siberia	50 °N–80 °N	60 °E–130 °E	88.9	99.8	99.4	100.0
AMA	Amazonia	30 °S–15 °N	90 °W–30 °W	97.1	100.0	89.2	100.0
CAF	Central Africa	20 °S–20 °N	25 °W–50 °E	83.6	99.7	60.2	94.5

scenes. To estimate the impact of this assumption, we have performed a limited number of simulated retrievals. For example, when applying the BESD/C retrieval algorithm to a combination of different AODs, CODs and CTHs (45 combinations) we found for the VEG50 scenario (i.e. vegetation albedo and SZA 50°) that the mean XCO$_2$ bias and its scatter (1σ) is -0.18 ± 0.27 ppm for CA aerosol (XCH$_4$: -1.11 ± 1.83 ppb). When generating the simulated CarbonSat observations assuming that the aerosol is OPAC "continental polluted" (CP), the biases are very similar as for CA aerosols: -0.14 ± 0.31 ppm for XCO$_2$ and -1.09 ± 1.69 ppb for XCH$_4$ (for the CP aerosol the errors are even somewhat smaller, but note that this is not a comparison between identical scenes because of the quality filtering). The main difference between the two aerosol types is that CP aerosols contain more "soot" (69 % compared to 54 % for CA) but less "water-soluble" aerosol (31 % compared to 46 % for CA). However, aerosols are highly variable and errors can be larger depending on

aerosol type. For example aerosol type "desert", which consists of much larger particles than CA and CP aerosols (composition: 87.1 % "water soluble", 11.7 % "mineral/nucleation mode", 1.1 % "mineral/accumulation mode"), the biases are 0.54 ± 0.40 ppm for XCO$_2$ and 2.63 ± 2.10 ppb for XCH$_4$ as determined using the version of the BESD/C algorithm and its parameter settings including filtering criteria as used in this publication. Here a clear tendency for a high bias can be observed. This is partly because of a high bias (outliers) for certain scenes which are not filtered out (i.e. detected) by the currently used quality-filtering scheme. Larger errors may also occur if the aerosol profile variability is not dominated by variability in the boundary layer (here: 0–2 km) but by variations in higher altitudes. For example, if we generate simulated CarbonSat observation with CP aerosols using extinction profiles which peak in the 2–4 km region, the biases are 0.41 ± 0.71 ppm for XCO$_2$ and 1.96 ± 3.16 ppb for XCH$_4$ (for the retrieval we assume, as usual, CA aerosols mainly

Fig. 12. Regional cumulative error distributions for the four regions United States of America (USA), Europe (EUR), China (CHI) and Australia (AUS) for July. Also listed for each region is the percentage of the individual CarbonSat observations in that region with a systematic error (SE) less than a given value (red for XCO$_2$, green for XCH$_4$).
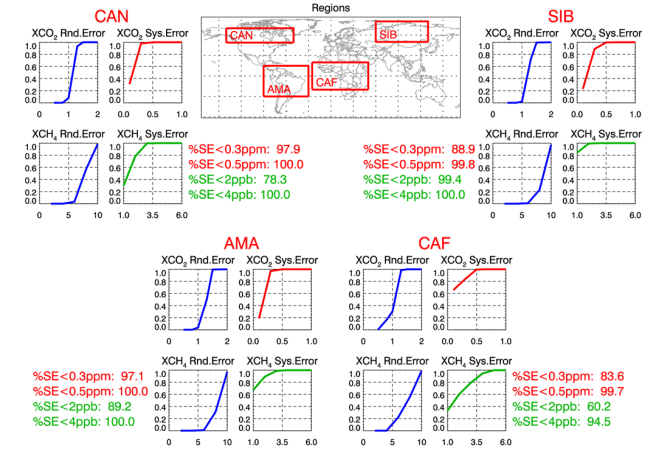

Fig. 13. As Fig. 12 but for the four regions Canada (CAN), Siberia (SIB), Amazonia (AMA) and central Africa (CAF).

in the 0–2 km region). This shows that aerosol (and cirrus) type and vertical profile variations cannot be neglected. This likely explains why the systematic errors for XCO$_2$ reported here are somewhat smaller compared to the errors reported in, for example, O'Dell et al. (2012) for GOSAT retrievals. The improved physical description of the above phenomena, or effects and their accommodation in the retrieval, will be the focus of subsequent research.

8 Conclusions

The objective of the CarbonSat mission is to improve our understanding of natural and anthropogenic sources and sinks of the two most important anthropogenic greenhouse gases (GHGs) carbon dioxide (CO$_2$) and methane (CH$_4$). One unique feature of CarbonSat is its "GHG imaging capability", which is achieved via a combination of high spatial resolution (2 km × 2 km) and good spatial coverage achieved by a relatively wide swath and no gaps between ground pixels. The width of the across-track swath has not yet been finally decided. Here we presented results for two swath widths: 240 km (CarbonSat's breakthrough requirement) and 500 km (goal requirement). This capability enables global imaging of localized strong emission sources, such as cities, power plants, methane seeps, landfills and volcanoes, and better disentangling of natural and anthropogenic GHG sources and sinks.

Source–sink information can be derived from the retrieved atmospheric column-averaged mole fractions XCO$_2$ and XCH$_4$ (Level 2 products) via inverse modelling. We have

presented an error analysis for CarbonSat XCO$_2$ and XCH$_4$ retrievals focusing on errors and performance issues related to non-linearity and interference errors (e.g. Connor et al., 2008) caused by clouds and aerosols. The results have been obtained using the BESD/C "full physics" (FP) retrieval algorithm and using the most recent instrument and mission specification.

Errors due to aerosols and thin cirrus clouds are expected to dominate the error budget especially for XCO$_2$ systematic errors. In order to quantify random and systematic errors, a one-year data set of simulated CarbonSat nadir mode observations over land has been generated and analysed. This has been achieved by developing an error parameterization scheme which permits fast computation of random and systematic XCO$_2$ and XCH$_4$ retrieval errors and averaging kernels. The method is based on applying the BESD/C FP algorithm to simulated CarbonSat observations. The resulting XCO$_2$ and XCH$_4$ errors and averaging kernels have been parameterized using a linear regression method.

We have focused on scattering-related errors obtained with the BESD/C FP retrieval method and using an error parameterization scheme which permits one to compute random and systematic errors for one year of simulated CarbonSat observations. Using this method, we have shown that systematic errors are mostly (approximately 85 %) below 0.3 ppm for XCO$_2$ (< 0.5 ppm: 99.5 %) and below 2 ppb for XCH$_4$ (< 4 ppb: 99.3 %). The single-measurement precision is typically 1.2 ppm for XCO$_2$ and 7 ppb for XCH$_4$ (1σ). For "proxy" (PR) retrievals, which are based on the retrieved CH$_4$-to-CO$_2$ column ratio (or its inverse, depending on application), it has been estimated that the systematic errors are about a factor of four smaller compared to FP retrievals but that the PR random errors are about 83 % larger for XCO$_2$ (2.2 ppm instead of typically 1.2 ppm for

FP retrievals) and about 28 % larger for $X\mathrm{CH}_4$ (9 ppb instead of typically 7 ppb). We also have shown that the number of quality-filtered observations per month over cloud- and ice-free land surfaces is in the range 33–46 million per month depending on season.

We have also shown that CarbonSat will provide valuable information on VCF retrieved from clear Fraunhofer lines located around 755 nm. We estimate that the VCF single-measurement precision is approximately $0.3\,\mathrm{mW\,m}^{-2}\,\mathrm{nm}^{-1}\,\mathrm{sr}^{-1}$ (1σ) at 755 nm. For GOSAT, Frankenberg et al. (2012) found that the achieved single-measurement precision is $0.5\,\mathrm{mW\,m}^{-2}\,\mathrm{nm}^{-1}\,\mathrm{sr}^{-1}$ (1σ) at 755 nm. According to Guanter et al. (2010), VCF retrieval errors less than about $0.5\,\mathrm{mW\,m}^{-2}\,\mathrm{nm}^{-1}\,\mathrm{sr}^{-1}$ would be valuable measurements as, for example, the expected signal variation at 760 nm is assumed to be in the range 0–$4\,\mathrm{mW\,m}^{-2}\,\mathrm{nm}^{-1}\,\mathrm{sr}^{-1}$. Systematic VCF errors as determined using the very fast but simple retrieval method presented here are typically less than $0.2\,\mathrm{mW\,m}^{-2}\,\mathrm{nm}^{-1}\,\mathrm{sr}^{-1}$. This systematic error estimate, however, does not include potential other error contributions such as intensity offsets (due to imperfect calibration). It also does not include possible errors due to rotational Raman scattering (RRS), which are expected to be small but may not be entirely negligible (Vasilkov et al., 2013).

The results presented here indicate that CarbonSat will be able to make significant contributions to improving our knowledge on the sources and sinks of these two very important GHGs. The data set presented here is currently being evaluated using global regional-scale inverse modelling to quantify this statement.

Finally, we have pointed out some of the limitations of the error parameterization method. Our scheme is more complex than previously used error parameterization schemes developed for other satellite missions (e.g. Hungershoefer et al., 2010) but is still quite simple. For example, aerosol type variations are neglected and it is assumed that aerosol variability is confined to the boundary layer. To better address these aspects will be a focus of our future activities.

As a first application, the data set has been used to assess the capability of CarbonSat to quantify the CO_2 emissions of large cities using Berlin, the capital of Germany, as an example (Buchwitz et al., 2013b). As shown in Buchwitz et al. (2013b), the precision of the inferred Berlin CO_2 emissions obtained from single CarbonSat overpasses is likely in the range 5–10 $\mathrm{MtCO}_2\,\mathrm{yr}^{-1}$ (10–20 %). As also shown in Buchwitz et al. (2013b), systematic errors can be of the same order depending on which assumptions are used with respect to observational systematic errors and (e.g. biogenic $X\mathrm{CO}_2$) modelling errors.

Appendix A

Consideration of terrestrial vegetation chlorophyll fluorescence (VCF)

Recently it has been shown that terrestrial VCF emission needs to be considered for accurate $X\mathrm{CO}_2$ retrieval (Frankenberg et al., 2012; Joiner et al., 2011). BESD/C has therefore been improved to consider this. As can be seen from Table 2, VCF is a state vector element for the version of BESD/C used in this study. In order to provide the radiative transfer model with a reasonable VCF first-guess value, a simple but very fast "dedicated VCF" (DVCF) retrieval scheme has been implemented. It is not based on full SCIATRAN computations but instead uses only a few constant pre-computed spectra (plus a low-order polynomial) to model the sun-normalized radiance by scaling these spectra using a simple but fast OE retrieval scheme. The method we use is similar to the methods described in Joiner et al. (2011) and Frankenberg et al. (2011).

The following spectra are used for DVCF pre-processing:

– A high-spectral-resolution solar irradiance spectrum. We use the "OCO Toon spectrum" described in O'Dell et al. (2012). This spectrum is the most important spectrum as required for VCF retrieval based on clear solar Fraunhofer lines.

– A low-order polynomial to consider spectrally broadband radiance variations due to, for example, aerosols, clouds and surface albedo or residual calibration issues.

– A surface emission VCF spectrum (Rascher et al., 2009). Note, however, that only a small spectral region is used by the DVCF algorithm (749–759 nm) and that the VCF spectrum is essentially constant (or varies only linearly) in this narrow spectral range and that therefore the retrieval results are essentially independent of the VCF spectrum used.

– A water vapour absorption spectrum computed offline with SCIATRAN using HITRAN 2008 spectroscopic line parameters (Rothman et al., 2009). Note that the underlying water absorption in the DVCF retrieval window is very weak and that including water absorption only slightly improves the quality of the spectral fit but hardly changes the retrieved VCF values.

These spectra are used at present by a simple but very fast non-iterative OE scheme to retrieve VCF essentially as a scaling factor of the VCF Jacobian. Atmospheric absorption and scattering are neglected by the currently implemented DVCF retrieval method.

A DVCF example fit is shown in Fig. A1. The CarbonSat nadir radiance (L: top panel a, black line) has been computed with the latest version of the SCIATRAN radiative
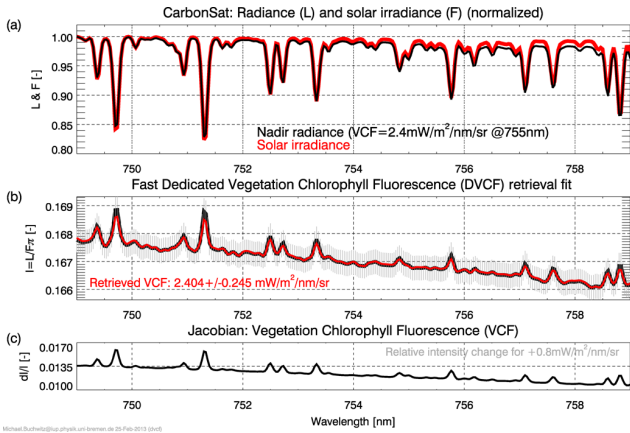
Fig. A1. Illustration of the CarbonSat BESD/C vegetation chlorophyll fluorescence (VCF) pre-processing step. **(a)** Nadir radiance spectrum (L: SZA 40°, vegetation albedo, black line) and solar irradiance (F: red line) normalized to their values at 749 nm. The difference is primarily due to VCF emission at the surface of 2.4 mW m^{-2} nm^{-1} sr^{-1} at 755 nm resulting in a difference of the slope and a "filling-in" of the solar Fraunhofer lines (most clearly visible for the two strong Fraunhofer lines located at 749.7 and 751.3 nm). **(b)** Simulated CarbonSat sun-normalized radiance ($I = L/F \cdot \pi$) measurement (black, with measurement error (grey vertical bars) and fitted VCF Jacobian – red, also shown separately in **(c)**. The retrieved VCF is 2.404 ± 0.245 mW m^{-2} nm^{-1} sr^{-1} (1σ).
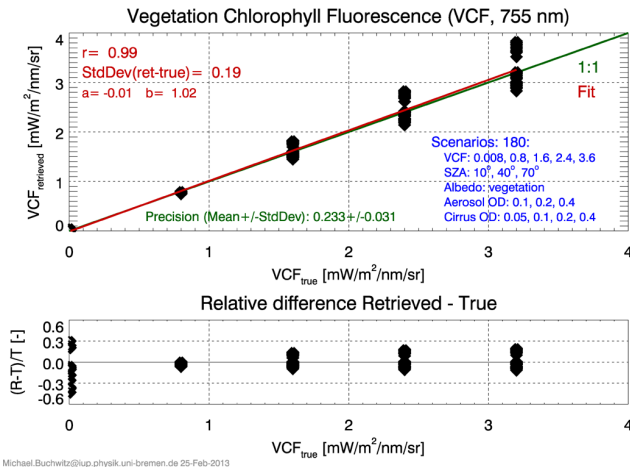
Fig. A2. Results of the dedicated VCF (DVCF) retrieval pre-processing step. Top: retrieved VCF (y axis) versus true VCF (x axis) for 180 scenarios as defined by VCF emission, SZA, and AOD and COD (see blue text for details). The linear correlation coefficient between the retrieved and the true VCF is $r = 0.99$. The standard deviation of the difference between the retrieved and true VCF is 0.19 mW m^{-2} nm^{-1} sr^{-1}. The random error (single observation precision) is 0.233 mW m^{-2} nm^{-1} sr^{-1} on average (standard deviation 0.031 mW m^{-2} nm^{-1} sr^{-1}). Bottom: relative difference between retrieved and true VCF as a function of the true VCF.
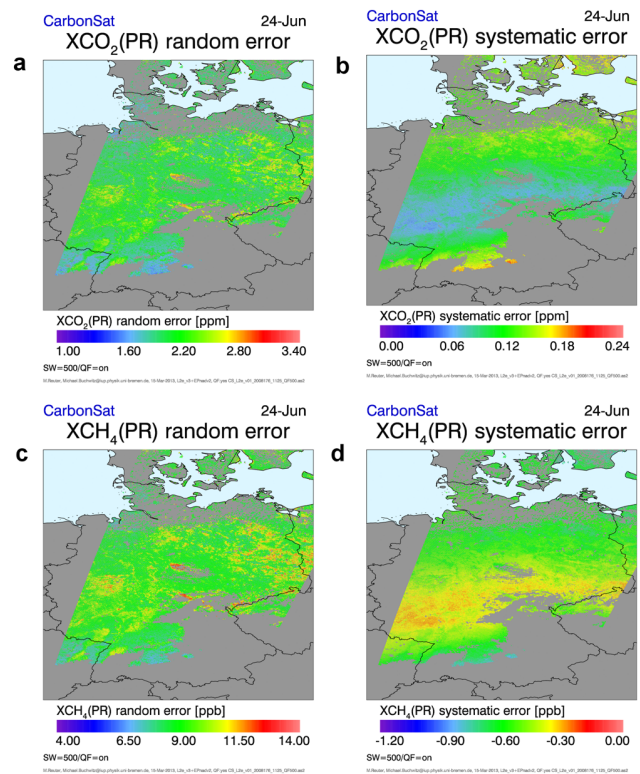

Fig. B1. As Fig. 7 but for "proxy" (PR) retrievals. As can be seen by comparison with Fig. 7, the random errors are larger (as two quite noisy retrievals are combined) but the systematic errors are much smaller, as many errors are common for CO_2 and CH_4 and therefore cancel if the ratio of the retrieved columns is computed.

transfer model, which takes all relevant processes including (multiple) scattering and surface emission by VCF into account. As can be concluded from the similarity between the (scaled) solar irradiance (F: top panel, red line) and the (scaled) nadir radiance, the spectral region used for DVCF retrieval is essentially free of atmospheric absorption features (even water vapour absorption is very small in this region). The difference between the two (scaled) spectra is primarily due to terrestrial vegetation fluorescence emission at the surface, which causes a (tiny) filling-in of the solar Fraunhofer lines (most clearly seen for the two strongest lines located at 749.7 and 751.3 nm) and a slope change over the spectral region (note that L and F have seen scaled to 1.0 at the lowest wavelength shown in Fig. A1). Panel b of Fig. A1 shows the corresponding sun-normalized radiance (black line) and its measurement error (1-σ noise level, grey vertical bars) and the fitted simple DVCF model (red line). As can be seen, the fit is good but not perfect. Especially the amplitude of the peaks do not match perfectly. This is due to the currently used fast and simple (e.g. non-iterative) DVCF model, which is not based on the full VCF Jacobian computed by SCIATRAN (note that SCIATRAN is not used for the DVCF
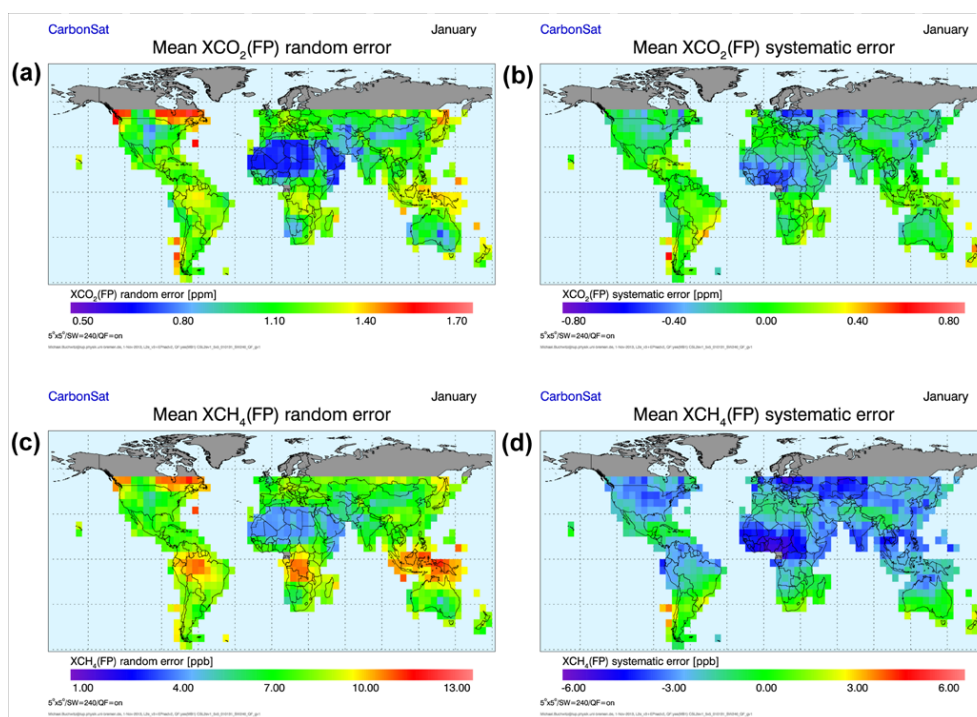
Fig. C1. As Fig. 9 but for January.

retrieval). As a result, the retrieved VCF is somewhat under-estimated for VCF values larger than the used a priori value (of $0.8\,\mathrm{mW\,m^{-2}\,nm^{-1}\,sr^{-1}}$) and overestimated for VCF values less than the used a priori value (at the a priori value the error is zero). The deviation is to a good approximation linear and scenario-independent, and therefore a simple linear correction is used. This can be improved using a more advanced algorithm, e.g. by using SCIATRAN for DVCF retrieval, but this would require more computational resources. For the purpose of this study, the currently implemented fast DVCF retrieval method is used. The retrieved VCF is used as a first-guess and a priori value for the full three-band BESD/C retrieval.

The DVCF retrieval method has been used to retrieve VCF from a large number of scenarios taking into account different SZA, aerosol amounts and cirrus parameters. Figure A2 shows the results for 180 scenarios (the parameters which have been varied are listed in Fig. A2; see blue text in panel a). As can be seen, a very good correlation between the retrieved and the true VCF exists ($r = 0.99$). As can also be seen, the standard deviation of the difference is $0.19\,\mathrm{mW\,m^{-2}\,nm^{-1}\,sr^{-1}}$ (less than approximately 20 % except for very low VCF emission; see panel b). Also listed is the single observation retrieval precision, which is $0.233 \pm 0.031\,\mathrm{mW\,m^{-2}\,nm^{-1}\,sr^{-1}}$ (mean and standard deviation as obtained from all 180 scenarios).

Appendix B

Proxy (PR) retrievals

For PR retrieval, the "dry air column" needed to convert the vertical column of the target gas (as given in, for example, number of molecules per cm^2) to a column-averaged mole fraction or mixing ratio (ppm or ppb) is not obtained from surface pressure (and the retrieved water column) but using a reference gas with a (approximately) known mixing ratio, here either CO_2 or CH_4, as already explained in Sect. 3. PR retrievals do not require the use of the O_2–A (i.e. NIR) band of CarbonSat. PR retrievals are essentially based on the retrieved column ratio of the two gases (times a correction factor). In order to estimate PR retrieval errors using given FP retrieval errors, the following approach can be used:

The ratio of XCH_4 / XCO_2 defines a conversion factor C between these two quantities, e.g. $C = 4.34\,\mathrm{ppb/ppm}$ ($= 1694.0\,\mathrm{ppb}/390.0\,\mathrm{ppm}$) for the model atmosphere used here. Using this conversion factor, and assuming that all errors are small (all relative errors are much smaller than 1.0, typically less than 0.01, as shown in this study), the XCO_2 random error for a PR retrieval is given by $\sqrt{\sigma_{CO_2,FP}^2 + (\sigma_{CH_4,FP}/C)^2}$, where $\sigma_{CO_2,FP}$ is the XCO_2 FP random error and $\sigma_{CH_4,FP}$ is the XCH_4 FP random error. The corresponding formula for the XCH_4 PR random error is $\sqrt{\sigma_{CH_4,FP}^2 + (\sigma_{CO_2,FP} \times C)^2}$. The XCO_2 PR systematic error

can be estimated via $\epsilon_{CO_2,FP} - \epsilon_{CH_4,FP}/C$, where the ϵ are the corresponding FP systematic errors. As can be seen from this formula, the XCO_2 PR error would be zero if the two systematic errors (after conversion of XCH_4 FP error to the corresponding XCO_2 error) were identical. For example, if the XCO_2 FP error is $+1\%$ ($+3.9$ ppm) and the XCH_4 FP error is also $+1\%$ ($+16.94$ ppb corresponding to $+3.9$ ppm after conversion), the XCO_2 PR error would be zero. If, however, in this case the XCH_4 error were -1% instead of $+1\%$, then the two errors would not cancel but instead amount to a $+2\%$ ($+7.8$ ppm) XCO_2 PR error. The XCH_4 PR systematic error can be estimated using an analogue formula via $\epsilon_{CH_4,FP} - \epsilon_{CO_2,FP} \times C$.

Figure B1 illustrates this. The "PR errors" shown Fig. B1 are the "FP errors" shown in Fig. 7 but converted to PR errors using the formulas given here. As can be seen, the PR random errors are larger than the FP errors, but the systematic PR errors are much smaller compared to the corresponding FP errors due to cancellation of errors, as expected. For the systematic XCO_2 errors the variation over the scene is only about 0.2 ppm, i.e. about a factor of four smaller compared to the FP errors. For XCH_4, the results are similar; the systematic XCH_4 PR error varies only about 1 ppb over the scene, which is also about four times smaller compared to the FP error. For random errors, the opposite is true: the PR random errors are about 83 % larger for XCO_2 (2.2 ppm instead of typically 1.2 ppm for FP retrievals) and about 28 % larger for XCH_4 (9 ppb instead of typically 7 ppb).

Appendix C

Monthly error maps for January

Figure C1 shows error maps for January. For a detailed description of the spatial resolution and assumed swath width, etc., please see the corresponding Fig. 9 for July.

References

Basu, S., Guerlet, S., Butz, A., Houweling, S., Hasekamp, O., Aben, I., Krummel, P., Steele, P., Langenfelds, R., Torn, M., Biraud, S., Stephens, B., Andrews, A., and Worthy, D.: Global CO_2 fluxes estimated from GOSAT retrievals of total column CO_2, Atmos. Chem. Phys., 13, 8695–8717, doi:10.5194/acp-13-8695-2013, 2013.

Bergamaschi, P., Frankenberg, C., Meirink, J. F., Krol, M., Villani, M. G., Houweling, S., Dentener, F., Dlugokencky, E. J., Miller, J. B., Gatti, L. V. Engel, A., and Levin, I.: Inverse modeling of global and regional CH_4 emissions using SCIA-MACHY satellite retrievals, J. Geophys. Res., 114, D22301, doi:10.1029/2009JD012287, 2009.

Bergamaschi, P., Houweling, H., Segers, A., Krol, M., Frankenberg, C., Scheepmaker, R. A., Dlugokencky, E., Wofsy, S. C., Kort, E. A., Sweeney, C., Schuck, T., Brenninkmeijer, C., Chen, H., Beck, V., and Gerbig, C.: Atmospheric CH_4 in the first decade of the 21st century: Inverse modeling analysis using SCIAMACHY satellite retrievals and NOAA surface measurements, J. Geophys. Res., 118, 7350–7369, doi:10.1002/jgrd.50480, 2013.

Boesch, H., Baker, D., Connor, B., Crisp, D., and Miller, C.: Global characterization of CO_2 column retrievals from shortwave-infrared satellite observations of the orbiting carbon observatory-2 mission, Remote Sens., 3, 270–304, doi:10.3390/rs3020270, 2011.

Bovensmann, H., Burrows, J. P., Buchwitz, M., Frerick, J., Noël, S., Rozanov, V. V., Chance, K. V., and Goede, A.: SCIAMACHY – mission objectives and measurement modes, J. Atmos. Sci., 56, 127–150, 1999.

Bovensmann, H., Buchwitz, M., Burrows, J. P., Reuter, M., Krings, T., Gerilowski, K., Schneising, O., Heymann, J., Tretner, A., and Erzinger, J.: A remote sensing technique for global monitoring of power plant CO_2 emissions from space and related applications, Atmos. Meas. Tech., 3, 781–811, doi:10.5194/amt-3-781-2010, 2010.

Buchwitz, M., de Beek, R., Burrows, J. P., Bovensmann, H., Warneke, T., Notholt, J., Meirink, J. F., Goede, A. P. H., Bergamaschi, P., Körner, S., Heimann, M., and Schulz, A.: Atmospheric methane and carbon dioxide from SCIAMACHY satellite data: initial comparison with chemistry and transport models, Atmos. Chem. Phys., 5, 941–962, doi:10.5194/acp-5-941-2005, 2005.

Buchwitz, M., Chevallier, F., and Bergamaschi, P.: User Requirements Document (URD) for the GHG-CCI project of ESA's Climate Change Initiative, Technical Report, 45 pp., version 1 (URDv1), 3 February 2011, available at: http://www.esa-ghg-cci.org (last access: 1 February 2013), 2011.

Buchwitz, M., Reuter, M., Schneising, O., Boesch, H., Guerlet, S., Dils, B., Aben, I., Armante, R., Bergamaschi, P., Blumenstock, T., Bovensmann, H., Brunner, D., Buchmann, B., Burrows, J. P., Butz, A., Chédin, A., Chevallier, F., Crevoisier, C. D.,

Deutscher, N. M., Frankenberg, C., Hase, F., Hasekamp, O. P., Heymann, J., Kaminski, T., Laeng, A., Lichtenberg, G., De Mazière, M., Noël, S., Notholt, J., Orphal, J., Popp, C., Parker, R., Scholze, M., Sussmann, R., Stiller, G. P., Warneke, T., Zehner, C., Bril, A., Crisp, D., Griffith, D. W. T., Kuze, A., O'Dell, C., Oshchepkov, S., Sherlock, V., Suto, H., Wennberg, P., Wunch, D., Yokota, T., and Yoshida, Y.: The Greenhouse Gas Climate Change Initiative (GHG-CCI): comparison and quality assessment of near-surface-sensitive satellite-derived CO_2 and CH_4 global data sets, Remote Sens. Environ., online first, doi:10.1016/j.rse.2013.04.024, 2013a.

Buchwitz, M., Reuter, M., Bovensmann, H., Pillai, D., Heymann, J., Schneising, O., Rozanov, V., Krings, T., Burrows, J. P., Boesch, H., Gerbig, C., Meijer, Y., and Löscher, A.: Carbon Monitoring Satellite (CarbonSat): assessment of scattering related atmospheric CO_2 and CH_4 retrieval errors and first results on implications for inferring city CO_2 emissions, Atmos. Meas. Tech. Discuss., 6, 4769–4850, doi:10.5194/amtd-6-4769-2013, 2013b.

Burrows, J. P., Hölzle, E., Goede, A. P. H., Visser, H., and Fricke, W.: SCIAMACHY – scanning imaging absorption spectrometer for atmospheric chartography, Acta Astronaut., 35, 445–451, 1995.

Butz, A., Hasekamp, O. P., Frankenberg, C., and Aben, I.: Retrievals of atmospheric CO_2 from simulated space-borne measurements of backscattered near-infrared sunlight: accounting for aerosol effects, Appl. Optics, 48, 3322, doi:10.1364/AO.48.003322, 2009.

Butz, A., Guerlet, S., Hasekamp, O., Schepers, D., Galli, A., Aben, I., Frankenberg, C., Hartmann, J.-M., Tran, H., Kuze, A., Keppel-Aleks, G., Toon, G., Wunch, D., Wennberg, P., Deutscher, N., Griffith, D., Macatangay, R., Messerschmidt, J., Notholt, J., and Warneke, T.: Toward accurate CO_2 and CH_4 observations from GOSAT, Geophys. Res. Lett., 38, L14812, doi:10.1029/2011GL047888, 2011.

Canadell, J. G., Ciais, P., Dhakal, S., Dolman, H., Friedlingstein, P., Gurney, K. R., Held, A., Jackson, R. B., Le Quéré, C., Malone, E. L., Ojima, D. S., Patwardhan, A., Peters, G. P., and Raupach, M. R.: Interactions of the carbon cycle, human activity, and the climate system: a research portfolio, Curr. Opin. Environ. Sustainabil., 2, 301–311, 2010.

Chevallier, F., Bréon, F.-M., and Rayner, P. J.: Contribution of the orbiting carbon observatory to the estimation of CO_2 sources and sinks: theoretical study in a variational data assimilation framework, J. Geophys. Res., 112, D09307, doi:10.1029/2006JD007375, 2007.

Ciais, P., Dolman, A. J., Bombelli, A., Duren, R., Peregon, A., Rayner, P. J., Miller, C., Gobron, N., Kinderman, G., Marland, G., Gruber, N., Chevallier, F., Andres, R. J., Balsamo, G., Bopp, L., Bréon, F.-M., Broquet, G., Dargaville, R., Battin, T. J., Borges, A., Bovensmann, H., Buchwitz, M., Butler, J., Canadell, J. G., Cook, R. B., DeFries, R., Engelen, R., Gurney, K. R., Heinze, C., Heimann, M., Held, A., Henry, M., Law, B., Luyssaert, S., Miller, J., Moriyama, T., Moulin, C., Myneni, R. B., Nussli, C., Obersteiner, M., Ojima, D., Pan, Y., Paris, J.-D., Piao, S. L., Poulter, B., Plummer, S., Quegan, S., Raymond, P., Reichstein, M., Rivier, L., Sabine, C., Schimel, D., Tarasova, O., Valentini, R., van der Werf, G., Wickland, D., Williams, M., and Zehner, C.: Current systematic carbon cycle observations and needs for implementing a policy-relevant

carbon observing system, Biogeosciences Discuss., 10, 11447–11581, doi:10.5194/bgd-10-11447-2013, 2013.

Cogan, A. J., Boesch, H., Parker, R., Feng, L., Palmer, P. I., Blavier, J.-F. L., Deutscher, N., Macatangay, R., Notholt, J., Roehl, C. M., Warneke, T., and Wunch, D.: Atmospheric carbon dioxide retrieved from the greenhouse gases observing satellite: comparison with ground-based TCCON observations and GEOS-Chem model calculations, J. Geophys. Res., 117, D21301, doi:10.1029/2012JD018087, 2012.

Connor, B. J., Bösch, H., Toon, G., Sen, B., Miller, C., and Crisp, D.: Orbiting Carbon Observatory: Inverse method and prospective error analysis, J. Geophys. Res., 113, 5305, doi:10.1029/2006JD008336, 2008.

Crisp, D., Atlas, R. M., Bréon, F.-M., Brown, L. R., Burrows, J. P., Ciais, P., Connor, B. J., Doney, S. C., Fung, I. Y., Jacob, D. J., Miller, C. E., O'Brien, D., Pawson, S., Randerson, J. T., Rayner, P., Salawitch, R. S., Sander, S. P., Sen, B., Stephens, G. L., Tans, P. P., Toon, G. C., Wennberg, P. O., Wofsy, S. C., Yung, Y. L., Kuang, Z., Chudasama, B., Sprague, G., Weiss, P., Pollock, R., Kenyon, D., and Schroll, S.: The Orbiting Carbon Observatory (OCO) mission, Adv. Space Res., 34, 700–709, 2004.

Crisp, D., Fisher, B. M., O'Dell, C., Frankenberg, C., Basilio, R., Bösch, H., Brown, L. R., Castano, R., Connor, B., Deutscher, N. M., Eldering, A., Griffith, D., Gunson, M., Kuze, A., Mandrake, L., McDuffie, J., Messerschmidt, J., Miller, C. E., Morino, I., Natraj, V., Notholt, J., O'Brien, D. M., Oyafuso, F., Polonsky, I., Robinson, J., Salawitch, R., Sherlock, V., Smyth, M., Suto, H., Taylor, T. E., Thompson, D. R., Wennberg, P. O., Wunch, D., and Yung, Y. L.: The ACOS CO_2 retrieval algorithm – Part II: Global XCO_2 data characterization, Atmos. Meas. Tech., 5, 687–707, doi:10.5194/amt-5-687-2012, 2012.

Dlugokencky, E. J., Bruhwiler, L., White, J. W. C., Emmons, L. K., Novelli, P. C., Montzka, S. A., Masarie, K. A., Lang, P. M., Crotwell, A. M., Miller, J. B., and Gatti, L. V.: Observational constraints on recent increases in the atmospheric CH_4 burden, Geophys. Res. Lett., 36, L18803, doi:10.1029/2009GL039780, 2009.

ESA (European Space Agency): ESA SP-1313/4, Candidate Earth Explorer Core Missions – Reports for Assessment: FLEX – Fluorescence Explorer, ESA Communication Production Office, Noordwijk, the Netherlands, available at: http://esamultimedia. esa.int/docs/SP1313-4_FLEX.pdf (last access: 1 February 2013), 2008.

Francey, R. J., Trudinger, C. M., van der Schoot, M., Law, R. M., Krummel, P. B., Langenfelds, R. L., Steele, L. P., Allison, C. E., Stavert, A. R., Andres, R. J., and Rödenbeck, C.: Atmospheric verification of anthropogenic CO_2 emission trends, Nat. Clim. Change, 3, 520–524, doi:10.1038/nclimate1817, 2013.

Frankenberg, C., Meirink, J. F., van Weele, M., Platt, U., and Wagner, T.: Assessing methane emissions from global spaceborne observations, Science, 308, 1010–1014, 2005.

Frankenberg, C., Butz, A., and Toon, G. C.: Disentangling chlorophyll fluorescence from atmospheric scattering effects in O_2 A-band spectra of reflected sun-light, Geophys. Res. Lett., 38, L03801, doi:10.1029/2010GL045896, 2011.

Frankenberg, C., O'Dell, C., Guanter, L., and McDuffie, J.: Remote sensing of near-infrared chlorophyll fluorescence from space in scattering atmospheres: implications for its retrieval and interfer-

ences with atmospheric CO_2 retrievals, Atmos. Meas. Tech., 5, 2081–2094, doi:10.5194/amt-5-2081-2012, 2012.

Guanter, L., Alonso, L., Gómez Chova, L., Meroni, M., Preusker, R., Fischer, J., and Moreno, J.: Developments for vegetation fluorescence retrieval from spaceborne high resolution spectrometry in the O_2 A and O_2 B absorption bands, J. Geophys. Res., 115, D19303, doi:10.1029/2009JD013716, 2010.

Guerlet, S., Basu, S., Butz, A., Krol, M., Hahne, P., Houweling, S., Hasekamp, O. P., and Aben, I.: Reduced carbon uptake during the 2010 Northern Hemisphere summer from GOSAT, Geophys. Res. Lett., 40, 2378–2383, doi:10.1002/grl.50402, 2013a.

Guerlet, S., Butz, A., Schepers, D., Basu, S., Hasekamp, O. P., Kuze, A., Yokota, T., Blavier, J.-F., Deutscher, N. M., Griffith, D. W. T., Hase, F., Kyro, E., Morino, I., Sherlock, V., Sussmann, R. S., Galli, A., and Aben, I.: Impact of aerosol and thin cirrus on retrieving and validating XCO_2 from GOSAT shortwave infrared measurements, J. Geophys, Res., 118, 4887–4905, doi:10.1002/jgrd.50332, 2013b.

Hess, M., Koepke, P., and Schult, I.: Optical properties of aerosols and clouds: the software package OPAC, B. Am. Meteorol. Soc., 79, 831–844, 1998.

Heymann, J., Schneising, O., Reuter, M., Buchwitz, M., Rozanov, V. V., Velazco, V. A., Bovensmann, H., and Burrows, J. P.: SCIAMACHY WFM-DOAS XCO_2: comparison with CarbonTracker XCO_2 focusing on aerosols and thin clouds, Atmos. Meas. Tech., 5, 1935–1952, doi:10.5194/amt-5-1935-2012, 2012a.

Heymann, J., Bovensmann, H., Buchwitz, M., Burrows, J. P., Deutscher, N. M., Notholt, J., Rettinger, M., Reuter, M., Schneising, O., Sussmann, R., and Warneke, T.: SCIAMACHY WFM-DOAS XCO_2: reduction of scattering related errors, Atmos. Meas. Tech., 5, 2375–2390, doi:10.5194/amt-5-2375-2012, 2012b.

Houweling, S., Krol, M., Bergamaschi, P., Frankenberg, C., Dlugokencky, E. J., Morino, I., Notholt, J., Sherlock, V., Wunch, D., Beck, V., Gerbig, C., Chen, H., Kort, E. A., Röckmann, T., and Aben, I.: A multi-year methane inversion using SCIAMACHY, accounting for systematic errors using TCCON measurements, Atmos. Chem. Phys. Discuss., 13, 28117–28171, doi:10.5194/acpd-13-28117-2013, 2013.

Hungershoefer, K., Breon, F.-M., Peylin, P., Chevallier, F., Rayner, P., Klonecki, A., Houweling, S., and Marshall, J.: Evaluation of various observing systems for the global monitoring of CO_2 surface fluxes, Atmos. Chem. Phys., 10, 10503–10520, doi:10.5194/acp-10-10503-2010, 2010.

Joiner, J., Yoshida, Y., Vasilkov, A. P., Yoshida, Y., Corp, L. A., and Middleton, E. M.: First observations of global and seasonal terrestrial chlorophyll fluorescence from space, Biogeosciences, 8, 637–651, doi:10.5194/bg-8-637-2011, 2011.

Kauss, J.: Aerosol-Parametrisierung für Strahlungstransport-Simulationen im ultravioletten bis nahinfraroten Spektralbereich, Diploma Thesis, available from: available at: http://www.iup.uni-bremen.de/sciamachy/NIR_NADIR_WFM_DOAS/kauss_dipl.pdf, University of Bremen, Institute of Environmental Physics, Bremen, Germany, 91 pp., 1998.

Keppel-Aleks, G., Wennberg, P. O., O'Dell, C. W., and Wunch, D.: Towards constraints on fossil fuel emissions from total column carbon dioxide, Atmos. Chem. Phys., 13, 4349–4357, doi:10.5194/acp-13-4349-2013, 2013.

Kirschke, S., Bousquet, P., Ciais, P., Saunois, M., Canadell, J. G., Dlugokencky, E. J., Bergamaschi, P., Bergmann, D., Blake, D. R., Bruhwiler, L., Cameron-Smith, P., Castaldi, S., Chevallier, F., Feng, L., Fraser, A., Heimann, M., Hodson, E. L., Houweling, S., Josse, B., Fraser, P. J., Krummel, P. B., Lamarque, J.-F., Langenfelds, R. L., Le Quéré, C., Naik, V., O'Doherty, S., Palmer, P. I., Pison, I., Plummer, D., Poulter, B., Prinn, R. G., Rigby, M., Ringeval, B., Santini, M., Schmidt, M., Shindell, D. T., Simpson, I. J., Spahni, R., Steele, L. P., Strode, S. A., Kengo Sudo, K., Szopa, S., van der Werf, G. R., Voulgarakis, A., van Weele, M., Weiss, R. F., Williams, J. E., and Zeng, G.: Three decades of global methane sources and sinks, Nat. Geosci., 6, 813–823, doi:10.1038/ngeo1955, 2013.

Kort, E. A., Frankenberg, C. F., Miller, C. E., and Oda, T.: Space-based observations of megacity carbon dioxide, Geophys. Res. Lett., 39, L17806, doi:10.1029/2012GL052738, 2012.

Krings, T., Gerilowski, K., Buchwitz, M., Reuter, M., Tretner, A., Erzinger, J., Heinze, D., Pflüger, U., Burrows, J. P., and Bovensmann, H.: MAMAP – a new spectrometer system for column-averaged methane and carbon dioxide observations from aircraft: retrieval algorithm and first inversions for point source emission rates, Atmos. Meas. Tech., 4, 1735–1758, doi:10.5194/amt-4-1735-2011, 2011.

Krings, T., Gerilowski, K., Buchwitz, M., Hartmann, J., Sachs, T., Erzinger, J., Burrows, J. P., and Bovensmann, H.: Quantification of methane emission rates from coal mine ventilation shafts using airborne remote sensing data, Atmos. Meas. Tech., 6, 151–166, doi:10.5194/amt-6-151-2013, 2013.

Kuze, A., Suto, H., Nakajima, M., and Hamazaki, T.: Thermal and near infrared sensor for carbon observation Fourier-transform spectrometer on the greenhouse gases observing satellite for greenhouse gases monitoring, Appl. Optics, 48, 6716–6733, doi:10.1364/AO.48.006716, 2009.

Leifer, I., Culling, D., Schneising, O., Farrell, P., Buchwitz, M., and Burrows, J. P.: Transcontinental methane measurements: Part 2: Mobile surface investigation of fossil fuel industrial fugitive emissions, Atmos. Environ., 74, 432–441, 2013.

Maksyutov, S., Takagi, H., Valsala, V. K., Saito, M., Oda, T., Saeki, T., Belikov, D. A., Saito, R., Ito, A., Yoshida, Y., Morino, I., Uchino, O., Andres, R. J., and Yokota, T.: Regional CO_2 flux estimates for 2009–2010 based on GOSAT and ground-based CO_2 observations, Atmos. Chem. Phys., 13, 9351–9373, doi:10.5194/acp-13-9351-2013, 2013.

McKain, K., Wofsy, S. C., Nehrkorn, T., Eluszkiewicz, J., Ehleringer, J. R., and Stephens, B. B.: Assessment of ground-based atmospheric observations for verification of greenhouse gas emissions from an urban region, P. Natl. Acad. Sci. USA, 109, 8423–8428, doi:10.1073/pnas.1116645109, 2012.

Meirink, J. F., Eskes, H. J., and Goede, A. P. H.: Sensitivity analysis of methane emissions derived from SCIAMACHY observations through inverse modelling, Atmos. Chem. Phys., 6, 1275–1292, doi:10.5194/acp-6-1275-2006, 2006.

National Research Council (NRC) – Committee on Methods for Estimating Greenhouse Gas Emissions, Verifying Greenhouse Gas Emissions: Methods to Support International Climate Agreements, 144 pp., available at: http://www.nap.edu/catalog/12883.html (last access: 1 February 2013), 2010.

O'Dell, C. W., Connor, B., Bösch, H., O'Brien, D., Frankenberg, C., Castano, R., Christi, M., Eldering, D., Fisher, B., Gunson, M.,

McDuffie, J., Miller, C. E., Natraj, V., Oyafuso, F., Polonsky, I., Smyth, M., Taylor, T., Toon, G. C., Wennberg, P. O., and Wunch, D.: The ACOS CO_2 retrieval algorithm – Part 1: Description and validation against synthetic observations, Atmos. Meas. Tech., 5, 99–121, doi:10.5194/amt-5-99-2012, 2012.

Olivier, J. G. J., Janssens-Maenhout, G., and Peters, J. A. H. W.: Trends in global CO_2 emissions, 2012 Report, PBL Netherlands Environmental Assessment Agency, The Hague, Joint Research Centre, Ispra, 2012.

Oshchepkov, S., Bril, A., Yokota, T., Morino, I., Yoshida, Y., Matsunaga, T., Belikov, D., Wunch, D., Wennberg, P., Toon, G., O'Dell, C., Butz, A., Guerlet, S., Cogan, A., Boesch, H., Eguchi, N., Deutscher, N., Griffith, G., Macatangay, R., Notholt, J., Sussmann, R., Rettinger, M., Sherlock, V., Robinson, J., Kyrö, E., Heikkinen, P., Feist, D. G., Nagahama, T., Kadygrov, N., Maksyutov, S., Uchino, O., and Watanabe, H.: Effects of atmospheric light scattering on spectroscopic observations of greenhouse gases from space: validation of PPDF-based CO_2 retrievals from GOSAT, J. Geophys. Res., 117, D12305, doi:10.1029/2012JD017505, 2012.

Rascher, U., Agati, G., Alonso, L., Cecchi, G., Champagne, S., Colombo, R., Damm, A., Daumard, F., de Miguel, E., Fernandez, G., Franch, B., Franke, J., Gerbig, C., Gioli, B., Gómez, J. A., Goulas, Y., Guanter, L., Gutiérrez-de-la-Cámara, Ó., Hamdi, K., Hostert, P., Jiménez, M., Kosvancova, M., Lognoli, D., Meroni, M., Miglietta, F., Moersch, A., Moreno, J., Moya, I., Neininger, B., Okujeni, A., Ounis, A., Palombi, L., Raimondi, V., Schickling, A., Sobrino, J. A., Stellmes, M., Toci, G., Toscano, P., Udelhoven, T., van der Linden, S., and Zaldei, A.: CEFLES2: the remote sensing component to quantify photosynthetic efficiency from the leaf to the region by measuring sun-induced fluorescence in the oxygen absorption bands, Biogeosciences, 6, 1181–1198, doi:10.5194/bg-6-1181-2009, 2009.

Rayner, P. J. and O'Brien, D. M.: The utility of remotely sensed CO_2 concentration data in surface inversions, Geophys. Res. Lett., 28, 175–178, 2001.

Reuter, M., Buchwitz, M., Schneising, O., Heymann, J., Bovensmann, H., and Burrows, J. P.: A method for improved SCIAMACHY CO_2 retrieval in the presence of optically thin clouds, Atmos. Meas. Tech., 3, 209–232, doi:10.5194/amt-3-209-2010, 2010.

Reuter, M., Bovensmann, H., Buchwitz, M., Burrows, J. P., Connor, B. J., Deutscher, N. M., Griffith, D. W. T., Heymann, J., Keppel-Aleks, G., Messerschmidt, J., Notholt, J., Petri, C., Robinson, J., Schneising, O., Sherlock, V., Velazco, V., Warneke, T., Wennberg, P. O., and Wunch, D.: Retrieval of atmospheric CO_2 with enhanced accuracy and precision from SCIAMACHY: validation with FTS measurements and comparison with model results, J. Geophys. Res., 116, D04301, doi:10.1029/2010JD015047, 2011.

Reuter, M., Bösch, H., Bovensmann, H., Bril, A., Buchwitz, M., Butz, A., Burrows, J. P., O'Dell, C. W., Guerlet, S., Hasekamp, O., Heymann, J., Kikuchi, N., Oshchepkov, S., Parker, R., Pfeifer, S., Schneising, O., Yokota, T., and Yoshida, Y.: A joint effort to deliver satellite retrieved atmospheric CO_2 concentrations for surface flux inversions: the ensemble median algorithm EMMA, Atmos. Chem. Phys., 13, 1771–1780, doi:10.5194/acp-13-1771-2013, 2013.

Rigby, M., Prinn, R. G., Fraser, P. J., Simmonds, P. G., Langenfelds, R. L., Huang, J., Cunnold, D. M., Steele, L. P., Krummel, P. B., Weiss, R. F., O'Doherty, S., Salameh, P. K., Wang, H. J., Harth, C. M., Mühle, J., and Porter, L. W.: Renewed growth of atmospheric methane, Geophys. Res. Lett., 35, L22805, doi:10.1029/2008GL036037, 2008.

Rodgers, C. D.: Inverse Methods for Atmospheric Sounding: Theory and Practice, World Scientific Publishing, River Edge, N.J., 2000.

Rothman, L. S., Gordon, I. E., Barbe, A., Benner, D. C., Bernath, P. E., Birk, M., Boudon, V., Brown, L. R., Campargue, A., Champion, J. P., Chance, K., Coudert, L. H., Dana, V., Devi, V. M., Fally, S., Flaud, J. M., Gamache, R. R., Goldman, A., Jacquemart, D., Kleiner, I., Lacome, N., Lafferty, W. J., Mandin, J. Y., Massie, S. T., Mikhailenko, S. N., Miller, C. E., Moazzen-Ahmadi, N., Naumenko, O. V., Nikitin, A. V., Orphal, J., Perevalov, V. I., Perrin, A., Predoi-Cross, A., Rinsland, C. P., Rotger, M., Simeckova, M., Smith, M. A. H., Sung, K., Tashkun, S. A., Tennyson, J., Toth, R. A., Vandaele, A. C., and Vander Auwera, J.: The HITRAN 2008 molecular spectroscopic database, J. Quant. Spectrosc. Ra., 110, 533–572, doi:10.1016/j.jqsrt.2009.02.013, 2009.

Rozanov, A., Rozanov, V., Buchwitz, M., Kokhanovsky, A., and Burrows, J. P.: SCIATRAN 2.0 – a new radiative transfer model for geophysical applications in the 175–2400 nm spectral region, Adv. Space Res., 36, 1015–1019, doi:10.1016/j.asr.2005.03.012, 2005.

Rozanov, V. and Kokhanovsky, A.: The solution of the vector radiative transfer equation using the discrete ordinates technique: selected applications, Atmos. Res., 79, 241–265, 2006.

Rozanov, V. V., Rozanov, A. V., Kokhanovsky, A. A., and Burrows, J. P.: Radiative transfer through terrestrial atmosphere and ocean: Software package SCIATRAN, J. Quant. Spectrosc. Ra., 133, 13–71, doi:10.1016/j.jqsrt.2013.07.004, 2014.

Schepers, D., Guerlet, S., Butz, A., Landgraf, J., Frankenberg, C., Hasekamp, O., Blavier, J.-F., Deutscher, N. M., Griffith, D. W. T., Hase, F., Kyro, E., Morino, I., Sherlock, V., Sussmann, R., and Aben, I.: Methane retrievals from Greenhouse Gases Observing Satellite (GOSAT) shortwave infrared measurements: performance comparison of proxy and physics retrieval algorithms, J. Geophys. Res., 117, D10307, doi:10.1029/2012JD017549, 2012.

Schneising, O., Buchwitz, M., Burrows, J. P., Bovensmann, H., Reuter, M., Notholt, J., Macatangay, R., and Warneke, T.: Three years of greenhouse gas column-averaged dry air mole fractions retrieved from satellite – Part 1: Carbon dioxide, Atmos. Chem. Phys., 8, 3827–3853, doi:10.5194/acp-8-3827-2008, 2008.

Schneising, O., Buchwitz, M., Reuter, M., Heymann, J., Bovensmann, H., and Burrows, J. P.: Long-term analysis of carbon dioxide and methane column-averaged mole fractions retrieved from SCIAMACHY, Atmos. Chem. Phys., 11, 2863–2880, doi:10.5194/acp-11-2863-2011, 2011.

Schneising, O., Heymann, J., Buchwitz, M., Reuter, M., Bovensmann, H., and Burrows, J. P.: Anthropogenic carbon dioxide source areas observed from space: assessment of regional enhancements and trends, Atmos. Chem. Phys., 13, 2445–2454, doi:10.5194/acp-13-2445-2013, 2013a.

Schneising, O., Reuter, M., Buchwitz, M., Heymann, J., Bovensmann, H., and Burrows, J. P.: Terrestrial carbon sink observed from space: variation of growth rates and seasonal cycle amplitudes in response to interannual surface temperature variability, Atmos. Chem. Phys. Discuss., 13, 22733–22755, doi:10.5194/acpd-13-22733-2013, 2013b.

Solomon, S., Qin, D., Manning, M., Chen, Z., Marquis, M., Averyt, K. B., Tignor, M., and Miller, H. L. (Eds.): Climate Change 2007: The Physical Science Basis, Contribution of Working Group I to the Fourth Assessment Report of the Intergovernmental Panel on Climate Change (IPCC), Cambridge University Press, 996 pp., 2007.

Stephens, B. B., Gurney, K. R., Tans, P. P., Sweeney, C., Peters, W., Bruhwiler, L., Ciais, P., Ramonet, M., Bousquet, P., Nakazawa, T., Aoki, S., Machida, T., Inoue, G., Vinnichenko, N., Lloyd, J., Jordan, A., Heimann, M., Shibistova, O., Langenfelds, R. L., Steele, L. P., Francey, R. J., and Denning, A. S.: Weak northern and strong tropical land carbon uptake from vertical profiles of atmospheric CO_2, Science, 316, 1732–1735, 2007.

Vasilkov, A., Joiner, J., and Spurr, R.: Note on rotational-Raman scattering in the O_2 A- and B-bands, Atmos. Meas. Tech., 6, 981–990, doi:10.5194/amt-6-981-2013, 2013.

Velazco, V. A., Buchwitz, M., Bovensmann, H., Reuter, M., Schneising, O., Heymann, J., Krings, T., Gerilowski, K., and Burrows, J. P.: Towards space based verification of CO_2 emissions from strong localized sources: fossil fuel power plant emissions as seen by a CarbonSat constellation, Atmos. Meas. Tech., 4, 2809–2822, doi:10.5194/amt-4-2809-2011, 2011.

Winker, D., Vaughan, M., Omar, A., Hu, Y., Powell, K. A., Liu, Z., Hunt, W., and Young, S.: Overview of the CALIPSO mission and CALIOP data processing algorithms, J. Atmos. Ocean. Tech., 26, 2310–2323, 2009.

Wunch, D., Wennberg, P. O., Toon, G. C., Keppel-Aleks, G., and Yavin, Y. G.: Emissions of greenhouse gases from a North American megacity, Geophys. Res. Lett., 36, L15810, doi:10.1029/2009GL039825, 2009.

Yoshida, Y., Ota, Y., Eguchi, N., Kikuchi, N., Nobuta, K., Tran, H., Morino, I., and Yokota, T.: Retrieval algorithm for CO_2 and CH_4 column abundances from short-wavelength infrared spectral observations by the Greenhouse gases observing satellite, Atmos. Meas. Tech., 4, 717–734, doi:10.5194/amt-4-717-2011, 2011.

Yoshida, Y., Kikuchi, N., Morino, I., Uchino, O., Oshchepkov, S., Bril, A., Saeki, T., Schutgens, N., Toon, G. C., Wunch, D., Roehl, C. M., Wennberg, P. O., Griffith, D. W. T., Deutscher, N. M., Warneke, T., Notholt, J., Robinson, J., Sherlock, V., Connor, B., Rettinger, M., Sussmann, R., Ahonen, P., Heikkinen, P., Kyrö, E., Mendonca, J., Strong, K., Hase, F., Dohe, S., and Yokota, T.: Improvement of the retrieval algorithm for GOSAT SWIR $X CO_2$ and $X CH_4$ and their validation using TCCON data, Atmos. Meas. Tech., 6, 1533–1547, doi:10.5194/amt-6-1533-2013, 2013.